TÉCNICO LISBOA

Mechanical Characterization of Wire Arc Additive Manufactured HSLA Steel

Luís Henrique de Araújo Gonçalves

Thesis to obtain the Master of Science Degree in

Aerospace Engineering

Supervisors: Prof. Virgínia Isabel Monteiro Nabais Infante
Dr. Daniel Filipe Oliveira Braga

Examination Committee

Chairperson: Prof. Filipe Szolnoky Ramos Pinto Cunha
Supervisor: Prof. Virgínia Isabel Monteiro Nabais Infante
Member of the Committee: Prof. Catarina Isabel Silva Vidal

January 2021

To my family

Declaration

I declare that this document is an original work of my own authorship and that it fulfills all the requirements of the Code of Conduct and Good Practices of the Universidade de Lisboa.

Acknowledgments

I would firstly like to thank Professor Virgínia Infante and Dr. Daniel Braga for proposing me this work and for all the support and guidance they gave me throughout this whole project.

To NOVA School of Science and Technology for the production and supply of WAAM specimens.

To Mr. Daniel, from the Laboratory of Material Characterization in IST, for helping me polishing my samples.

To Diogo Rechena, for the assistance with the Siemens NX software.

Also, to the various laboratory technicians and university workshops workers that simplified many aspects of this project.

To my friends, who were always by my side during this academic journey.

My profound gratitude to my family, specially my parents, Manuela and Carlos, for their support, kindness and for their efforts with providing me the best education possible.

Also, to the FCT projects PTDC/EME-EME/29340/2017—DisFri and PTDC/EME-EME/29339/2017 – MIAMI for the provided fundings.

Resumo

Na indústria aeroespacial, existe uma constante procura por alternativas mais rápidas, baratas e sustentáveis. O fabrico aditivo, mais especificamente *Wire and Arc Additive Manufacturing*, surge como competidor viável aos métodos mais tradicionais, apresentando grande potencial para produção de peças, principalmente de grandes dimensões, para uma variedade de materiais. Algumas desvantagens estão relacionadas com o fraco desempenho mecânico e a má qualidade da superfície do material depositado. Uma compreensão mais profunda sobre este processo é necessária, visto ainda permanecer bastante inexplorado. Neste trabalho, foram fabricadas paredes WAAM de aço HSLA utilizando duas entregas térmicas distintas com o objetivo de estudar o seu impacto no desempenho mecânico dos provetes. Os resultados mostraram que esta teve influência no desempenho mecânico dos provetes, com o conjunto de baixa entrega térmica a apresentar uma microestrutura mais refinada e maiores valores de extensão máxima e dureza. Poucas diferenças foram notórias para as várias localizações dos provetes nas paredes. Em relação aos ensaios de fadiga, e embora o número de provetes ensaiados tenha sido reduzido, foi observada uma grande dispersão de resultados. Fenómenos como o endurecimento secundário podem ter contribuído para isso e estudos futuros deverão focar-se na sua investigação. A medição do campo de deformações durante os ensaios de tracção com a correlação digital de imagem (DIC) permitiram verificar a concentração de tensões em defeitos pontuais que levaram à ruptura dos provetes. Estes modos de falha foram comprovados nas análises de fractografia e o comportamento mecânico foi comparado com modelos numéricos sem a presença de defeitos.

Palavras-chave: WAAM, fabrico aditivo, desempenho mecânico, entrega térmica

Abstract

In the aerospace industry, there is a continuous demand for faster, cheaper, and more sustainable options. Additive manufacturing, more specifically Wire and Arc Additive Manufacturing, emerges as a viable competitor to more traditional methods, showing the great potential of being used in part production. This technique allows the creation of large geometry parts for a variety of materials. Some disadvantages are related to the poor mechanical performance and surface quality of the deposited material. However, a deeper understanding of this process is still needed as it remains fairly unexplored. In this work, HSLA steel WAAM wall structures were manufactured using two different heat inputs with the aim of studying its impact on the specimens' mechanical performance. Results showed that it had some influence on the specimen's mechanical performance, with the Lower Heat input set presenting a more refined microstructure and higher values of maximum strain and hardness. Little differences were spotted regarding the various specimen heights along the wall. Regarding fatigue life tests, and despite the small number of specimens tested, a large dispersion of results was observed. Phenomena such as secondary hardening may have contributed to this and future studies should focus on their investigation. Strain field measurement during the tensile tests with digital image correlation (DIC) allowed the verification of stress concentration areas in specific defects that led to the rupture of the specimens. These failure modes were verified in the fractography analysis and the mechanical behavior was compared with numerical models without the presence of defects.

Keywords: Additive Manufacturing, WAAM, mechanical performance, heat input

Contents

List of Tables

List of Figures

Acronyms and Symbols

Acronyms

AD **A**s-**D**eposited

AF **A**cicular **F**errite

AM **A**dditive **M**anufacturing

ASTM **A**merican **S**ociety for **T**esting and **M**aterials

CAD **C**omputer **A**ided **D**esign

CPU **C**entral **P**rocessing **U**nit

DC **D**irect **C**urrent

DED **D**irected **E**nergy **D**eposition

DIC **D**igital **I**mage **C**orrelation

EDM **E**lectric **D**ischarge **M**achining

FCT **F**aculdade de **C**iências e **T**ecnologia

FEMFAT **F**inite **E**lement **M**ethod **F**atigue

FEM **F**inite **E**lement **M**odeling

FE **F**inite **E**lement

FGF **F**ine-**G**rain **F**errite

FSP **F**errite **S**ide **P**late

GMAW **G**as **M**etal **A**rc **W**elding

GTAW **G**as **T**ungsten **A**rc **W**elding

HCF **H**igh **C**ycle **F**atigue

HH **H**igh **H**eat

HSLA **H**igh-**S**trength **L**ow **A**lloy

IST **I**nstituto **S**uperior **T**écnico

LCF **L**ow **C**ycle **F**atigue

LH **L**ow **H**eat

MIG **M**etal **I**nert **G**as

NASA **N**ational **A**eronautics and **S**pace **A**dministration

PAW **P**lasma **A**rc **W**elding

PBF **P**owder **B**ed **F**usion

PF **P**ro-eutectoid **F**errite

S-N **S**tress-**N**umber of cycles to failure

SEM **S**canning **E**lectron **M**icroscope

ST **S**olution **T**reatment

UNL **U**niversidade **N**ova de **L**isboa

UTS **U**ltimate **T**ensile **S**trength

VIC **V**isual **I**mage **C**orrelation

WAAM **W**ire and **A**rc **A**dditive **M**anufacturing

WFR **W**ire **F**eed **R**ate

YS **Y**ield **S**tress

Greek symbols

ϵ Strain

ν Poisson's Ratio

σ_U Ultimate Tensile Strength

σ_{max} Maximum Stress

σ_{min} Minimum Stress

σ_{yield} Yield Strength

Symbols

a Base

b Middle

c Top

E	Young's Modulus
H	High
L	Low
N	Number of Fatigue Cycles
R	Stress Ratio
S	Maximum Applied Stress
x, y, z	Cartesian Components.

Chapter 1

Introduction

1.1 Motivation

In the aerospace industry, as well as other transport engineering sectors, there is a continuous search for cheaper, lighter, and more sustainable materials that can present better or similar mechanical performances than the already existent ones. The techniques used to mold them are also a subject of constant improvement, with several options being presented to the manufacturers. New methods try to present ways of speeding up the manufacturing process and at the same time reducing the production costs and complexity while keeping the same reliability.

The environmental impact of the adopted methods and materials is also of great relevance. Fuel consumption might be the most influential aspect, influencing the sustainability of the product. Additionally, traditional and widely used subtractive methods, like milling, leave out a lot of material remains at the end of the process that are not utilized. Additive methods present a viable alternative to this issue.

Additive manufacturing (AM) has been experiencing an exponential growth in the past decades. Its cost-effective approach and versatility make it a strong candidate for many industrial applications. The ability to produce complex geometry parts and the range of materials that can be processed with it are the main strong points of this method category. However, its reliability and performance are still of big concern [1].

From the technologies used in the AM of metallic alloys the most common ones are those based on laser. Laser metal deposition and selective laser melting are examples. Others, such as Wire and Arc Additive Manufacturing (WAAM), based on electric arc, have been investigated and are shown to be competitive with the first ones. Low fabrication times, ability to produce large parts and low capital investment are just a few perks of WAAM [2].

A deeper understanding of this process is still in need. Fatigue lifetime and surface quality as well as the mechanical performance of the produced parts require special attention. Additionally, certification of WAAM parts needs to be performed as it is slowing down a wider use of this technology [2].

1.2 Objectives

The main objective of this dissertation is to study the mechanical performance of HSLA steel specimens produced by Wire and Arc Additive Manufacturing. In order to do this the following steps were taken:

- Produce several HSLA steel thin wall structures using WAAM technology, with different heat input values;
- Characterize the produced specimens, according to their location on the wall structure and the heat input to which they were subjected, by analysing their microstructure and determining their mechanical properties.

1.3 Thesis Outline

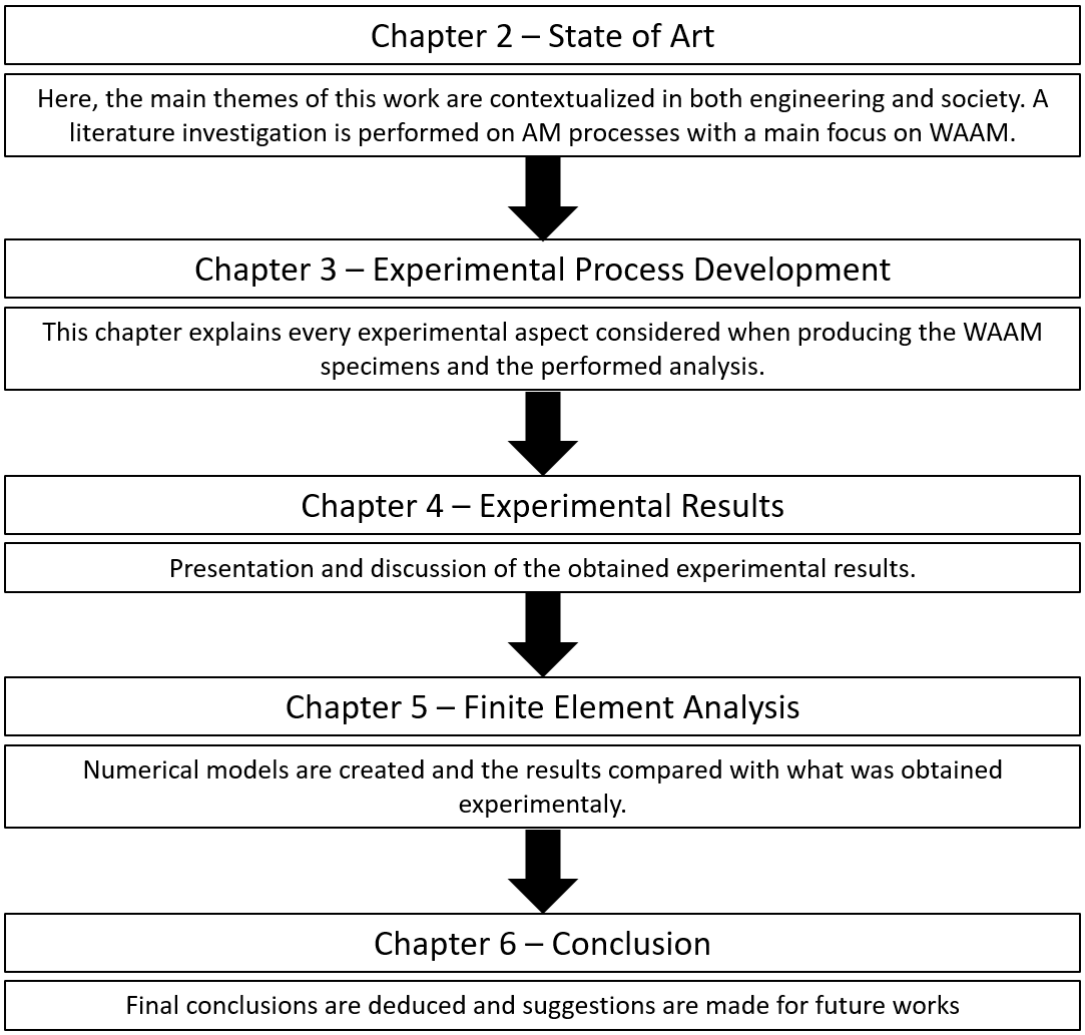

Figure 1.1: Thesis Outline Diagram

Chapter 2

State of Art

In this chapter, a general analysis is presented on Additive Manufacturing (AM) with a special focus on Wire and Arc Additive Manufacturing (WAAM). This is followed by a detailed vision of the performance of its components, especially regarding tensile properties and fatigue resistance. References from several scientific publications are utilized to uphold the mentioned topics.

2.1 Wire and Arc Additive Manufacturing

WAAM is a metal 3D printing technology that holds a huge potential for large-scale 3D printing applications across multiple industries [3]. This AM method enables the creation of parts by melting and fusing material as it is deposited and can also be used for repairing operations and rebuilding damaged components. Cheaper processes and materials, comparing with other AM techniques, as well as the strong mechanical properties of the obtained products are just the main advantages of this method [4]. WAAM supports a large range of metals, such as stainless steel; nickel-based alloys; titanium alloys; and aluminum alloys, with the condition that they come in wire form.

Given this description and the fact that this process is still relatively unexplored it became an appealing object of study for this dissertation.

2.2 Evolution of AM Processes and Applications

The first use of Additive Manufacturing processes can be traced back almost 150 years, with photosculptures and freeform topographical maps being built from two-dimensional layers [5]. During the 20^{th} century, the invention of the computer and Computer-Aided Design (CAD) helped to power AM growth, with an increase in patents and academic publications being recorded in the '80s and early '90s.

With the constant advance of technology, AM processes evolved and began being used to produce patterns, tooling, and final parts. Currently, AM products and services are used in several activities, including energy, transportation, manufacturing, art, architecture, space exploration, and military [5]. Involving various methods, materials, and equipment. Figure 2.1 shows a 36,000 kg WAAM hook,

designed specifically for offshore lifting operations. Figure 2.2 shows a NASA rocket nozzle printed with the Blown Powder Directed Energy Deposition technique.

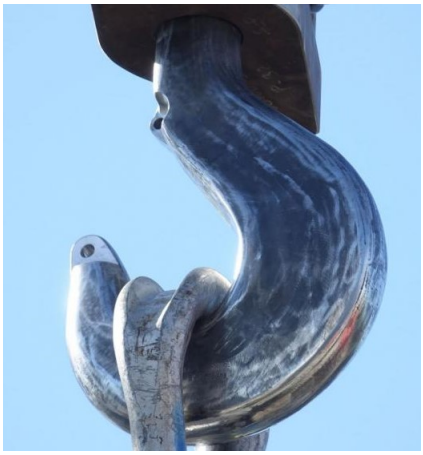

Figure 2.1: 3D printed WAAM hook, adapted from [6]

Figure 2.2: 3D printed nozzle, adapted from [7]

The evolution of these processes is justified by several advantages over other traditional methods, which include the fabrication of complex geometry with high precision, customization, and maximum material optimization. There are also no added costs regarding mold making and tooling for a customized product [8].

AM is capable of fabricating parts of various sizes, but the precision each one is made with depends on the accuracy of the chosen method and the scale of printing. An example of that is micro-scale 3D printing, which faces issues with its resolution, layer bonding, and surface finish. Fabrication speed and high costs remain the bigger challenges to mass production usage of this method [8, 9].

2.3 Additive Manufacturing using metals

AM methods can be classified according to the nature and the aggregate state of the feedstock as well as the binding mechanism between the joined layers of material. In the case of AM of metals, a powder or wire of the chosen material is melted by the energy input of a laser or electron beam. The

melted material is transformed, layer by layer, into a solid part of the intended geometry [10].

When printing metals, the most popular techniques currently used are Powder Bed Fusion (PBF) and Direct Energy Deposition (DED). Other methods, such as cold spraying and friction stir deposition (FSD), are also available [8].

The first one, PBF, consists of very thin layers of powder being spread and closely packed on a platform. These layers are fused together with a binder or a laser beam. Selective Laser Sintering (SLS) and Selective Laser Melting (SLM) are two examples of PBF methods.

DED processes are characterized by using an energy source, typically a laser, electron beam, or an electrical arc, to melt the feedstock material (powder or wire) while also melting a small targeted region of the substrate [8].

Figure 2.3 presents a visual representation of the different metal AM processes.

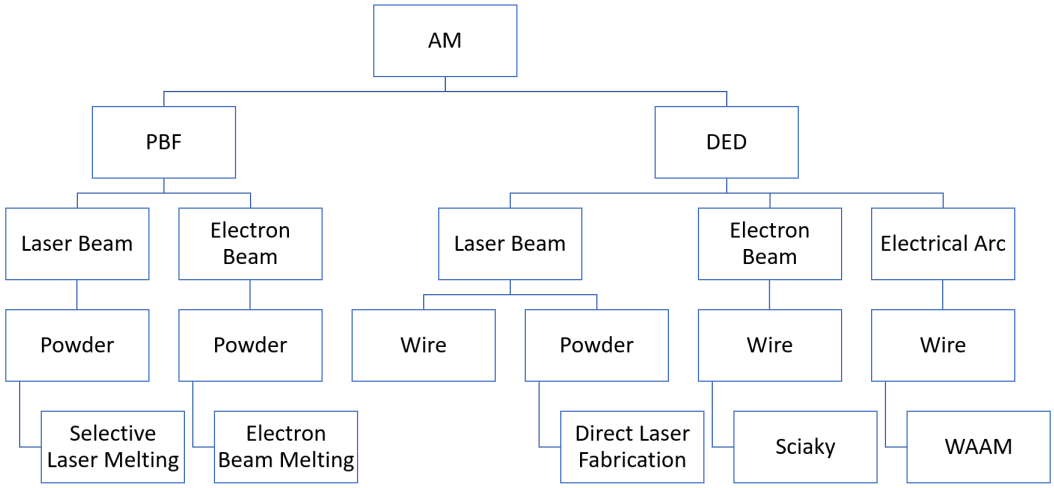

Figure 2.3: Metal AM processes, adapted from [11].

When intensively comparing both methods, one can note that DED presents higher speeds and lower manufacturing times and costs. However, some limitations can be encountered in its mechanical performance and surface quality. This means it is primarily used on large and low complexity parts, while PBF is ideal for printing more complex structures that require fine resolution and high surface quality (which depends on the size of the powder grains). The time and cost of the operation are major setbacks of this method [8, 10].

2.4 Overview of the Wire and Arc Additive Manufacturing (WAAM) Process

The combination of an electric arc as a heat source and wire as feedstock is the basis of this DED process. The robotic arm of a WAAM machine has greater freedom of movement when compared to PBF methods. This, allied with the process's efficient material utilization, high deposition rate, and low equipment cost, enables the production of large yet simple parts with subsequent low environmental impact [12]. Also, the WAAM system was found to reduce fabrication time by 40-60% and post-machining

time by 15-20%, depending on the size of the component, when compared to traditional subtractive manufacturing [13].

The WAAM process consists of building parts by staking layers of beads thanks to an electric arc that melts a wire of the intended material [14]. This method can be used to produce large parts for several applications, such as aerospace, naval, and power generation, as well as to add details on existing parts originally manufactured through other processes. It is also useful to repair worn-out features or damaged parts by depositing new material on their surface, avoiding the need to produce a new part from scratch, resulting in significant cost savings.

Despite this, major issues such as surface uncleanness, residual stresses, distortion due to excessive heat and less precision, results in stair-stepping, hindering the stabilization of the process [15].

There are three WAAM based techniques, that differ on the heat source: Gas Metal Arc Welding (GMAW), Gas Tungsten Arc Welding (GTAW), and Plasma Arc Welding (PAW). The choice of which technique to use is going to influence the processing conditions and production rate of the component. The first one presents higher deposition rates, that range from 2-3 kg/hr to 6-8 kg/hr, in comparison with the other two, 1-2 kg/hr for GTAW and 2-4 kg/hr for PAW [13]. GMAW is better when working with aluminum and steel but in the case of titanium the deposited material mechanical properties are not satisfactory and its surface shows high roughness due to arc wandering. This makes PAW and GTAW more suitable to work with this metal [15]. Additionally, GMAW shows poor stability and generates spatter and fumes due to the electric current being directly applied on the feedstock. On the other hand, in PAW and GTAW, the wire is not fed coaxially which can affect the metal deposition consistency [13, 14].

Figure 2.4 shows a scheme representing the GMAW process.

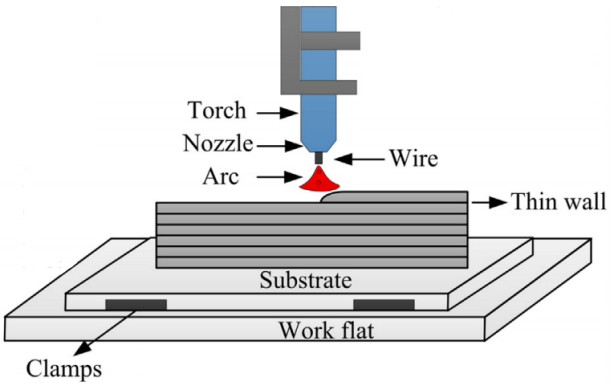

Figure 2.4: Schematic illustration of WAAM-GMAW, adapted from [16].

2.4.1 Process Parameters

To produce the best possible results with the WAAM process, one should take into account the influence of the various key parameters involved. Wire Feed Rate (WFR), Travel Speed, Arc Current, Argon Flow Rate, Printing Path Strategy, Heat Input, and Pre-heating are considered to have a major impact on the final component's stability and performance. This can be witnessed in the bead shape and size, bead roughness, melt through depth, wetting angle, oxidation levels, and microstructure of the part [15].

Wire Feed Rate shows a linear variation with bead height. When WFR is high, the bead will be tall and narrow. Roughness and melt through depth are considered to be independent from it [15].

Regarding Travel Speed, bead width, melt through depth, and wetting angle are shown to decrease when this parameter increases. On the other hand, bead roughness has a slight increase [17].

Arc Current mostly impacts bead roughness, with its increase provoking a reduction in the value of the latter. It also causes the wetting angle, bead width, and melt through depth to increase.

A smart strategy should be adopted with respect to the amount of Heat Input during the welding process. A higher input allows the deposition of more material but less with less accuracy, in what regards the quality of the surface. An exaggerated input will remelt the previously deposited layers, leading to a deterioration of the bead geometry, microstructure, and even affect the mechanical properties. In some extreme cases, it can cause the burn-off of the material and penetration of the substrate. Despite this, insufficient input also presents some setbacks: uneven deposition, unfused layers, and more spatter. The wiser approach suggested by literature is to decrease the heat input, around 5-20%, between each layer deposited, to avoid excesses. The reduction value will depend on the material used and geometry of the part [17, 18]. This Heat Input strategy can be achieved by raising the travel speed for each layer while keeping the arc current constant.

It is also important to take into account the effect of the huge temperature difference between the bead and the substrate. This will cool down the molten metal before fine and uniform distribution of carbides takes place, leading to a columnar grain structure in the bead. To diminish this, the pre-heating of the substrate is advised as it will ensure a decrease in the temperature gradient and help achieve a fine grain formation, and consequently leading to better mechanical properties [15, 19].

The way each layer is deposited can affect the geometry of the part. If all layers are printed in the same direction, a high point at the end and a low point at the beginning of the weld are formed. By depositing each layer in a different direction from the previous one, this effect can be reduced. This is called the zig-zag technique.

2.4.2 Microstructure

Grain structure control is very important in this process since it heavily influences the mechanical properties of the fabricated part. During WAAM, the deposited material undergoes multiple heating and cooling cycles that result in unique morphologies and microstructures.

WAAM parts' microstructures usually consist of large columnar grains formed by epitaxial growth from the substrate, along the maximum temperature gradient. This typically follows the building direction, perpendicular to the solid/liquid interface [20]. The main issue with this type of growth is the resulting anisotropic properties, which can be a major setback in multi-axial loading conditions.

Equiaxed grains are proved to be more advantageous, as they can reduce cracking tendency while improving ductility, resulting in parts with near isotropic properties. To obtain them, in-process and post-processing heat treatments are fundamental. The pre-heating of the substrate is recommended since the temperature difference verified between the substrate and the bead (mentioned in section 2.4.1) powers the formation of a columnar grain structure.

A deeper understanding of grain refinement was studied by Easton et al. [21].

Dai et al. [22] analyzed the microstructure and mechanical properties of a high-strength low alloy (HSLA) steel. Relatively to its microstructure, the results showed that it can be divided into four regions: solidification zone; complete austenitizing zone; partial austenitizing zone; and tempering zone. These zones exist simultaneously in the sublayers of the deposited layer, where they undergo different thermal cycles which will lead to distinct microstructures. This will severely affect the mechanical properties of the part.

The solidification zone presents columnar crystals, generated along with the direction of the highest cooling rate, and an extremely high cooling speed. The microstructure of this zone is composed of pro-eutectoid ferrite (PF), ferrite side plate (FSP), and acicular ferrite (AF) grains. This last one is ideal for enhancing the strength and toughness of the steel.

In the complete austenitizing zone, the average grain size is smaller than in the solidification zone. Here, columnar crystals have become unclear and some equiaxed grains emerge. The microstructure of this zone is composed of lower percentages of PF and FSP and higher AF when compared with the solidification zone, as well as a small percentage of fine-grain ferrite (FGF). As the temperature decreases, there is an increase in AF and FGF.

In the partial austenitizing zone, columnar grains disappeared giving way to more refined equiaxed grains. There are less PF, FSP, and AF and more FGF when compared with the two previously described zones.

Finally, the tempering zone shows fine equiaxed grains, smaller than in the partial austenitizing zone. Its microstructure is composed of FGF.

In this study, it was also observed that during the rapid heating process ferrite transformed into austenite. However, some ferrite nuclei remained in the austenite grains. When the cooling cycle happens, the presence of these nuclei promotes the formation of FGF. Also, after the deposition of several layers, some supercooled austenite remains in the tempering zone, due to the rapid cooling.

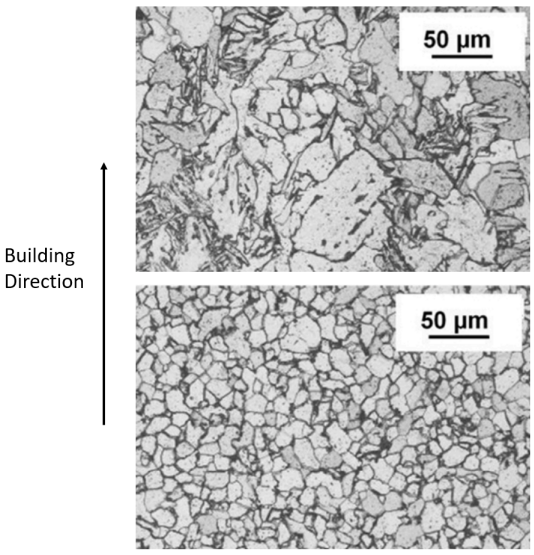

Figure 2.5: Microstructure of two different WAAM wall locations, adapted from [23].

Rodrigues et al. [24] investigated the microstructure and mechanical properties of WAAM HSLA steel parts and their correlation with the heat input variation. In their observations, heat accumulation and consequent low cooling rates were shown to favour grain growth, meaning the parts built with a higher heat input presented larger grains, and the grain size increased along with the height of the produced walls.

The same phenomenon was documented by E. Aldalur et al. [23], with grain size variations being observed along the wall structure. Figure 2.5 shows the microstructure of two different locations on the constructed wall. The bottom image corresponding to a low height and the top image corresponding to a high height. The previously mentioned grain refinement difference can be verified.

2.4.3 Challenges associated with WAAM

Despite all the advantages previously mentioned, this method faces some setbacks in the components' fabrication. The main challenges encountered have to do with residual stresses, distortion, porosity, surface quality, cracking and delamination. Some issues are material-specific, like the case of bad surface roughness in steel, porosity in aluminum alloys, and oxidation in titanium alloys [15]. Unstable weld pool dynamics due to poor parameter setup, bad programming strategy, thermal deformation, environmental influence, and other machine malfunctions can also be the cause of these defects.

2.4.3.1 Residual Stresses and Distortion

The presence of residual stresses and distortion on a WAAM part is, as for all the other methods, impossible to completely prevent. These can be a result of the thermal contraction caused by the multiple heating and cooling cycles that the material undergoes. Residual stresses can lead to distortion and reduction of fatigue performance, fracture resistance and, if sufficiently high, can even influence the mechanical properties of the part. According to W. J. Sames et al. [25], cracking will take place if the value for the residual stress is higher than the UTS of the material. Also, if the value is lower than the UTS but higher than the YS, warping or plastic deformation will occur.

It was stated, by J. Ding et al. [26], that residual stress is uniformly distributed along the deposited wall and that the residual stress from a deposited layer had little effect on the following ones. However, when the part was released from the clamps, internal stresses were redistributed with a much higher value at the bottom of the part (in the interface with the substrate) than at the top. This caused bending distortion of the part.

There are many techniques that try to minimize the impact of residual stresses and deformations in WAAM. Mughal et al. [27] studied the influence that process parameters can have on the residual stresses distribution in a GMAW deposition. Different sequences and rates of deposition were found to significantly affect this distribution as well as the magnitude of deformations. Layers starting from outside to the center was the strategy with the lowest impact on the final parts.

Another method used to reduce residual stresses is called Interpass cold rolling [28] which consists of consecutive rolling of each layer after deposition. It helps reduce residual stresses, distortion, and bring homogeneous material properties. The roller travels horizontally, parallel to the surface, inducing

plastic deformation by the compression enforced perpendicularly to the substrate. With the presence of a thermal gradient, alternative re-heating, and re-cooling, there is an evolution in the anisotropic material structure and microstructure. This technique is also found to effectively reduce microstructural anisotropy.

2.4.3.2 Porosity

Porosity can have severe implications on the mechanical properties of the material. This defect can be subdivided into two types: raw material-induced and process-induced. The first one has to do with WAAM's raw material - feedstock wire and substrate - and surface contaminants, e.g. grease, moisture, dust particles, and other hydrocarbon compounds. These are very difficult to completely remove and when not, are absorbed into the molten pool and will generate porosity after solidification [15, 29]. Taking this into account, extra attention should be paid when dealing with the cleanliness of raw materials.

Process-induced porosity can be caused by an unstable deposition process, poor path planning, or an improper shielding. These might lead to insufficient fusion or spatter injection which consequently creates gaps or voids in the workpiece [13].

R. Biswal et al. [30] studied the effect of internal porosity on the fatigue strength of a wire and arc additive manufactured titanium alloy. In their tests, two types of specimens were compared, a first one, which served as the control group, without porosity, and a second one with induced porosity utilizing contaminated wires. The results revealed similar static strength between the two groups however, fatigue strength was 33% lower for the porosity group. Elongation also suffered, with the second group having a 66% lower result than the first.

2.4.3.3 Cracks and Delamination

Another crucial challenge is the formation of cracks and delamination. For these, material characteristics and thermal signature of the process are both responsible. Cracks can be subdivided in two categories: grain boundary cracks and solidification cracks. The first type is usually formed around grain boundaries due to the differences between boundary morphology and potential precipitate formation or dissolution. The second type is caused by high strain in the molten pool or the obstruction of solidified grain flow, mainly depending on the material solidification nature [15].

Delamination is a visible and irreversible defect, not being reparable by post-processing treatments. It occurs due to inappropriate deposition temperature or insufficient re-melting of the underlying solid between layers.

J. Gu et al. [31] studied the cracking susceptibility of the WAAM process for Al-Cu-Mg alloys. The main objective of this study was to understand how to minimize cracks during deposition. For this, the influence of heat input, composition, microstructure, and mechanical properties were considered. It was first observed that microcracks were usually caused by a lack of eutectics and propagated at the inter-layer equiaxed grain zone.

Alloy's composition was found to have a major impact on cracking susceptibility. Alloys with 4.2-6.3% of Cu and 0.8-1.5% of Mg were less vulnerable to cracking than others. In addition, a higher

wire feed rate, for the same travel speed, was translated into a higher heat input but a lower density of the deposited material, which significantly increased cracking tendency. Finally, higher microhardness lowered crack vulnerability due to the existence of finer grains, which help to suppress cracks.

2.4.4 General Mechanical Properties

2.4.4.1 Hardness

Hardness is found to be directly related to the material's microstructure level of homogeneity [23]. The decreasing refinement observed in WAAM structure as the distance from the substrate increases, see section 2.4.2, should be translated into diminishing values of hardness. In a previously mentioned study [24], coarser grains in the top part of the wall structure led to lower values of hardness, which increased as the height decreased. Figure 2.6 shows such results.

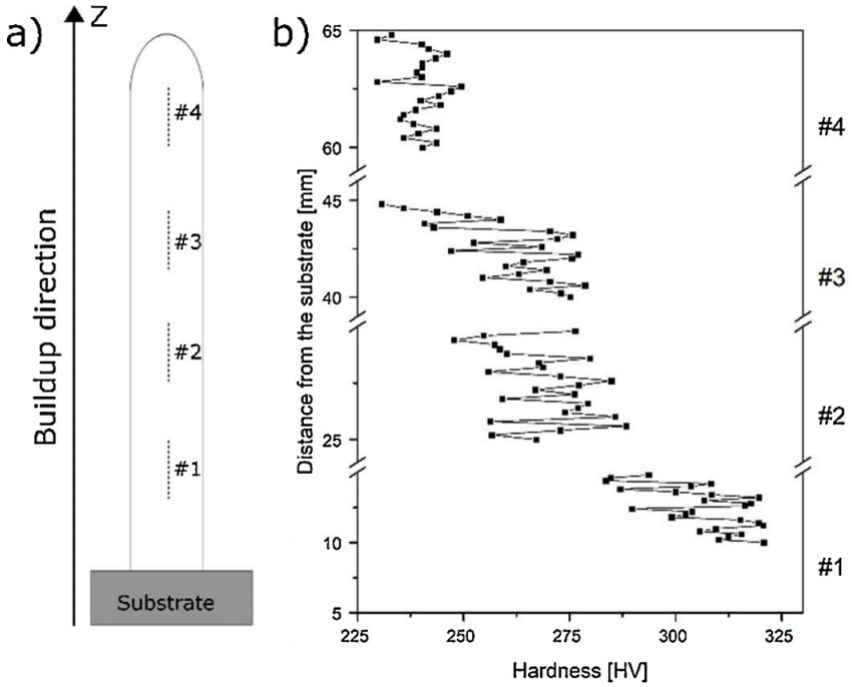

Figure 2.6: Hardness profile along a WAAM HSLA steel wall, adapted from [24].

2.4.4.2 Tensile Strength

Tensile strength commonly depends on the microstructure of the component formed during the additive process, as well as its density. AM fabricated parts present a finer microstructure when compared to others produced via traditional processes, which consequently means that they evidence higher tensile strength [10].

As mentioned in section 2.4.2, the microstructure of the fabricated part is inevitably anisotropic with respect to the building direction. This means that tensile properties, such as UTS, can also present anisotropic behaviour.

Caballero et al. [32] studied the effect of different WAAM variables on microstructure and mechanical

properties (YS, UTS, and elongation) of 17-4 PH Stainless steel specimens. Four different treatments were given to the samples: as-deposited (AD); as-deposited plus solution treatment (1040ºC for 30 min) (AD+ST); as-deposited plus H900 aging treatment (480ºC for 1 h) (AD+H900); and as-deposited followed by solution treatment and H900 aging treatment (ST+H900). The best overall results were obtained for the last treatment, which guaranteed a homogeneous microstructure. Regarding orientation-specific behaviors, results showed some differences in terms of strength and elongation. However, only UTS showed deviations and only in AD and AD+H900. This anisotropic response was related to the columnar microstructure of these specimens.

In a different article, Wang et al. [33] investigated the macrostructure, microstructure, and mechanical properties of a Ti-6Al-4V alloy after WAAM deposition. They observed that there was no correspondence between the position of the sample in the wall and its tensile strength however, sample orientation had a significant influence. The average UTS, YS, and strain to failure for the horizontal direction (parallel to the substrate) of the specimens were, respectively: 1033 MPa; 950 MPa; and 11.7%. In comparison, for the vertical direction, UTS was 918 MPa and YS was 803 MPa. Given the small differences between directions, the tensile properties were considered to be only slightly anisotropic. To also take into account that the average strength of a forged bar of the same material was 10% higher than the deposited part.

Gordon et al [34] observed that, for horizontally orientated specimens (parallel to the substrate) of stainless steel 304, there was no statistical difference in the tensile properties as a function of the height of the build.

As for the study performed by T. A. Rodrigues et al. [24], for a HSLA steel, similar values of UTS and elongation to fracture were reported along the height of the wall, suggesting homogeneity of mechanical properties.

2.4.4.3 Fatigue Strength

WAAM has found various applications in some industrial sectors, such as aeronautics and space. These are important examples of how crucial a good fatigue performance of the required components is for the well functioning and safety of the parts and structures involved. The primary concern for AM methods is the fatigue life compared to wrought, however, this property's experimentation is very demanding due to being time-consuming and adequate statistical data requiring a lot of tests that involve various conditions.

Fatigue strength of a component, identically to static strength, heavily depends on the material's microstructure. Other variables, such as material defects and surface roughness also play an important role in the fatigue life of the given part. The presence of defects, induced during the manufacturing process, can significantly reduce the fatigue life of a component in comparison to the expected. This is because the initial phases of fatigue damage, micro-cracks and slip-bands formation, are already initiated or even completed. Porosity and insufficient layer bonding will increase scatter of the experimental results, making it more difficult to obtain a decent estimate of the fatigue life [10, 35]. Surface roughness can be seen as already initiated micro-cracks, having a similar role in fatigue performance. Surface treatments, like polishing, can diminish its impact.

Regarding fatigue life prediction, there are three different approaches documented: statistical; notch fatigue method; and fracture mechanics approach [30]. The first type is characterized by the prediction of fatigue life by using the initial distribution of porosity obtained from X-ray computed tomography. Weibull's weakest-link fatigue assessment is an example [36]. This approach is not suitable for wire-based AM processes as they exhibit fewer and isolated voids. The classic notch fatigue method treats porosity as a stress raiser. Naturally, the probability of fatigue crack initiating in a weak spot of the material, where more stresses are present, is higher. A study [37] based on this method, implemented in the FEMFAT fatigue post-processor, stated that using the average stress acting on a finite volume in the notch root, that is subjected to stress level greater than 90% of the maximum stress, showed better fatigue life prediction accuracy. The fracture mechanics approach assumes that there are preexisting cracks in the component or are initiated early in its life. This method states that the fatigue life of a component is determined by the rate of growth of these cracks under cyclic loading.

The previously mentioned study, performed by Wang et al. [33], also investigated the fatigue behavior of WAAM Ti-6Al-4V alloy specimens. Results showed that the majority of both vertical and horizontally orientated specimens presented a better fatigue life than the baseline material. On the other hand, a small number of specimens failed at an early stage, which was caused by trapped gas pores due to contamination of the wire during deposition. After a closer look at the surface of the prematurely failed specimens, there were signs of fatigue cracks initiated very close to the material's surface. In this study, specimens' orientation and location were not a decisive factor in their fatigue life. The results, however, were inconclusive because there was an insufficient number of data.

A study by Dirisu et al. [38] presented surface waviness as a major contributor to the decrease of fatigue life of a WAAM steel component. Also, the effect of compressive residual stress on the mechanical behaviour of the as-deposited steel was achieved using a process that combines deposition and rolling on the component's surface. It was showed that in fact, surface waviness deeply affects the fatigue life and mechanical strength of the WAAM component. Also, rolling was shown to improve the overall mechanical properties, in particular fatigue life, of the part by plastically deforming the surface grooves and increasing the notch radius, hence minimizing stress concentration effects.

2.5 Chapter Resume

A brief summary about AM methods was presented, showing their evolution, characteristics, applications, and the wide range of different techniques where WAAM is included.

From the referenced literature, it is possible to understand how innovative and efficient WAAM is and how impactful it can be to the industrial world. Its characteristics, regarding the type of feedstock and heat source, were also particularized with respect to other AM methods.

Some setbacks were also mentioned, mainly poor surface quality and residual stresses of the fabricated parts, which can be improved with post-processing methods and intensive research.

For the experimental phase of this work, several considerations could be taken into account. When analysing the microstructure, the presence of elongated grains is expected as well as the evolution of

the microstructure along with the height of the wall with decreasing grain refinement. Mechanical properties can be substantially affected by the type of microstructure the built wall presents and the different parameters chosen. Also, not to forget the influence that possible voids and surface imperfections might have in the final results for mechanical properties.

Chapter 3

Experimental process development

This chapter covers every detail of the experimental process, such as material properties, equipment used, including welding and testing machines, set of parameters and other important procedures. The parameters adopted during the production of the specimens were based on previous similar works [24]. To investigate the mechanical properties and quality of the obtained material it was necessary to perform a variety of mechanical tests. After this was accomplished and the results were analysed, a discussion on them could be made.

3.1 Material

The feedstock material proposed for this work was the AWS A5.28 ER110S-G. This HSLA steel was used in the wire form with a diameter of 1 mm. For the fatigue specimens walls a wire with a diameter of 1.2 mm was used due to lack of stock by the supplier. Tables 3.1 and 3.2 present its chemical composition and mechanical properties, respectively.

Table 3.1: AWS A5.28 ER110S-G chemical composition [39].

C [%]	Si [%]	Mn [%]	P [%]	S [%]	Cu [%]
0.1	0.9	1.8	$<$0.015	$<$0.015	$<$0.25

Cr [%]	Ni [%]	Mo [%]	Al [%]	Zr + Ti [%]	Fe [%]
0.5	2.10	0.55	$<$0.10	$<$0.15	Balance

Table 3.2: AWS A5.28 ER110S-G mechanical properties [39].

UTS [MPa]	Yield Stress [MPa]	Elongation % on 5d
980	890	19

Note that these properties are referent to the base material, which is in wire form. The deposited material, as is going to be shown in further sections, might have different properties.

This material was proposed for this work due to being suitable for welding of low-alloy steels with very high mechanical properties. It is used in the building, transports, naval, aerospace, and other industries [39].

3.2 Welding Machine

The experimental apparatus used in this work was the custom-built WAAM-GMAW equipment existent in the industrial technology laboratories of FCT-UNL, see Figure 3.1, that consisted of a customized welding torch mounted on a three-axis positioning system, with a working envelope of 2760 x 1960 x 2000 mm. To deposit the material over the substrate, a welding machine from KEMPY, with a power source Pro MIG 3200, wire feeder, and control unit Pro MIG 501 was used. The mild steel substrates, where the walls were built on, had dimensions of 250 x 100 x 10 mm and were cleaned and dried before the experiment. These dimensions were kept constant to guarantee similar building conditions for all walls, also helping in avoiding distortions and different heat dissipation conditions.

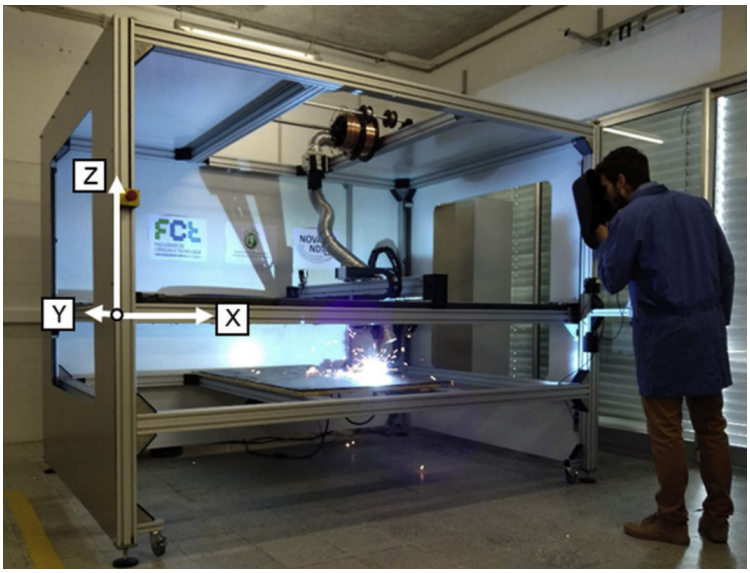

Figure 3.1: WAAM welding machine, adapted from [24].

3.3 Experimental Procedure

3.3.1 Produced Walls

The walls produced in this study had a length of 180 mm and the contact-tip-to-work distance was set to 7 mm. The dwell time between the deposited layers was kept constant at one minute. All experiments used a continuous-wave mode with the electrode connected to the positive terminal (DC+).

There were two different sets of walls produced, the first had a Low Heat (LH) input and the second a High Heat (HH) input . These were obtained by varying the travel speed of the process while the voltage, current, and wire feed speed were kept constant for both sets. Table 3.3 presents the values for these deposition parameters.

The shielding gases used were pure Ar (99.999%) and a mixture of Ar + 1% CO2 + 18% He at a flow rate of 8 and 16 l/min for sets HH and LH, respectively.

In the material deposition, for every layer deposited the torch ascended to a height equal to the bead

Table 3.3: Process Parameters.

Sample	Voltage [V]	Current [A]	Wire Feed Speed [mm/s]	Travel Speed [mm/s]	Heat Input [J/mm]
LH	21	95	3	9	221
HH	21	95	3	3.9	511

height. The deposition strategy adopted was the zig-zag, which consisted on inverting the direction of deposition of each layer, promoting a more levelled structure in terms of height. This process was repeated until a height of approximately 100 mm was reached. These dimensions were specified in favour of the required number of tests and considering the fixture and the tool diameter. As already mentioned, these parameters were based on previous similar works [24].

3.3.2 Specimens

For this study, 6 Low Heat input and 3 High Heat input walls were fabricated. The first 3 of each set were used in the uniaxial tensile tests and the remaining 3 of the LH input set were used in the fatigue tests.

Specimens were obtained from the produced walls by Electrical discharge machining (EDM), according to the ASTM A370 standard, see Figure 3.2. The machine used for this process was the ONA AF35.

For every wall there are 3 different specimen locations: base (a); middle (b); and top(c). Table 3.4 summarizes all specimens produced in this work according to their heat input, location and purpose. In Figure 3.3 a simple scheme represents the 3 different specimen locations.

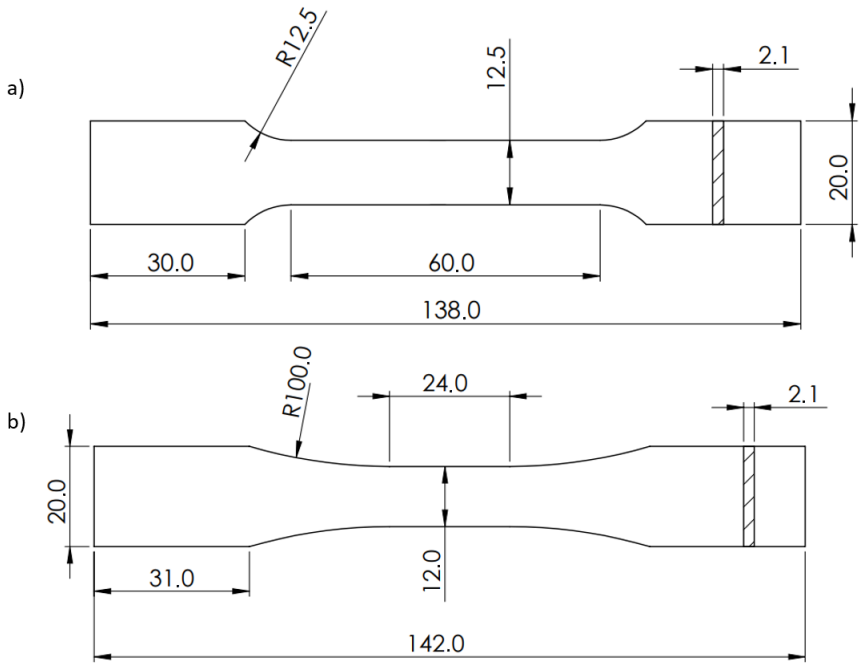

Figure 3.2: Specimen dimensions: a) tensile; b) fatigue.

Table 3.4: Specimens Produced.

Specimen Tag	Wall	Heat Input [L/H]	Location [a/b/c]	Test
1La	1	L	a	Tensile - DIC
1Lb	1	L	b	Tensile - DIC
1Lc	1	L	c	Tensile - DIC
2La	2	L	a	Tensile - Clip-gage
2Lb	2	L	b	Tensile - Clip-gage
2Lc	2	L	c	Tensile - Clip-gage
3La	3	L	a	Tensile - Clip-gage
3Lb	3	L	b	Tensile - Clip-gage
3Lc	3	L	c	Tensile - Clip-gage
4Ha	4	H	a	Tensile - DIC
4Hb	4	H	b	Tensile - DIC
4Hc	4	H	c	Tensile - DIC
5Ha	5	H	a	Tensile - Clip-gage
5Hb	5	H	b	Tensile - Clip-gage
5Hc	5	H	c	Tensile - Clip-gage
6Ha	6	H	a	Tensile - Clip-gage
6Hb	6	H	b	Tensile - Clip-gage
6Hc	6	H	c	Tensile - Clip-gage
8La	8	L	a	Fatigue Tensile
8Lb	8	L	b	Fatigue Tensile
8Lc	8	L	c	Fatigue Tensile
9La	9	L	a	Fatigue Tensile
9Lb	9	L	b	Fatigue Tensile
9Lc	9	L	c	Fatigue Tensile
10La	10	L	a	Fatigue Tensile
10Lb	10	L	b	Fatigue Tensile
10Lc	10	L	c	Fatigue Tensile

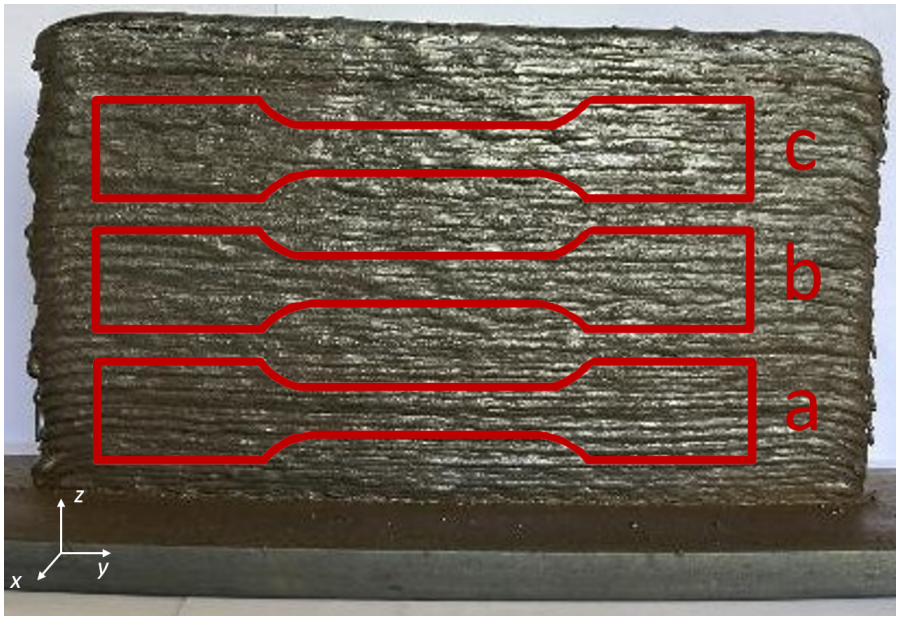

Figure 3.3: WAAM wall structure with specified specimen locations

3.4 Microstructure Analysis

In order to perform the microscopy analysis, it was necessary to prepare the specimens beforehand. The samples were cut and fitted into molds that were filled with epoxy resin mixed with hardener (with a

25:3 ratio).

After a 24 hour curing process, the samples underwent a treatment that consisted on polishing the material with sandpaper of increasing grades (240-320-500-1000-2000-4000) and finally using a 3 μm and 1 μm diamond compound polishers. All of this was performed in an automatic polisher, monitoring the surface evolution with an optical microscope. The samples were also repeatedly submerged in water where ultrasound treatment helped remove impurities.

Finally, the polished surface was contrasted with reagent (Nital 3%) for a few seconds to highlight grain boundaries.

The microscopy observation was conducted on specimens belonging to the LH input set and and the HH input set. Also, two different locations were accessed, base (a) and middle (b). In each of them the three faces, one in each direction, were analysed.

The microscope used for the microstructure observation was the OLYMPUS CK40M, at room temperature, with increasing magnification values, see Figure 3.4.

Figure 3.4: OLYMPUS CK40M microscope

3.5 Hardness Tests

The hardness examination aids the mechanical and microstructural characterization of the weld. For every sample, 5 measurements were made along a line with a 1 mm distance separating each indentation. In total, 4 specimens were tested, 2 belonging to the Low Heat input set and 2 belonging to the High Heat input. For each one, 3 faces, one in each direction were subjected to examination.

The machine used was the AVK-C2 Hardness Tester and the applied load was 2 kgf for 10 seconds,

for each indentation, at room temperature. Figure 3.5 shows the machine used for the microhardness tests as well as a sample being tested and the microscopic view of the Vickers indentation.

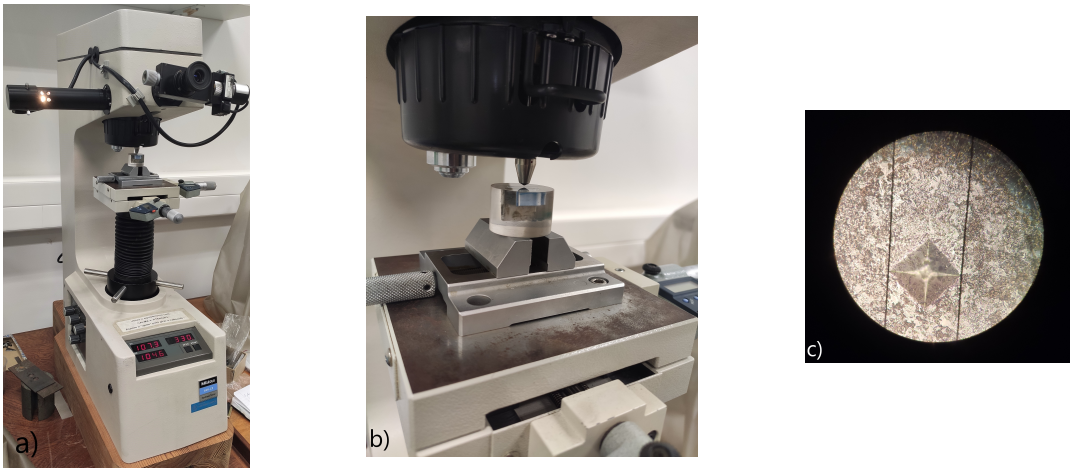

Figure 3.5: a) AVK-C2 Hardness Tester; b) A sample being indented; c) Microscopic view of the Vickers indentation.

3.6 Tensile Tests

In order to determine the tensile mechanical properties of the produced specimens, uniaxial tensile strength tests were performed. These tests were carried out at IST using the INSTRON® 3369 with 50 kN maximum load capacity, at room temperature. The cross-head speed was set to 1 mm/min.

During these tests, the displacement was measured either using a clip-gage, with an initial length of 25 mm, or the DIC equipment. Figure 3.6 shows the testing machine and a specimen with a placed clip-gage.

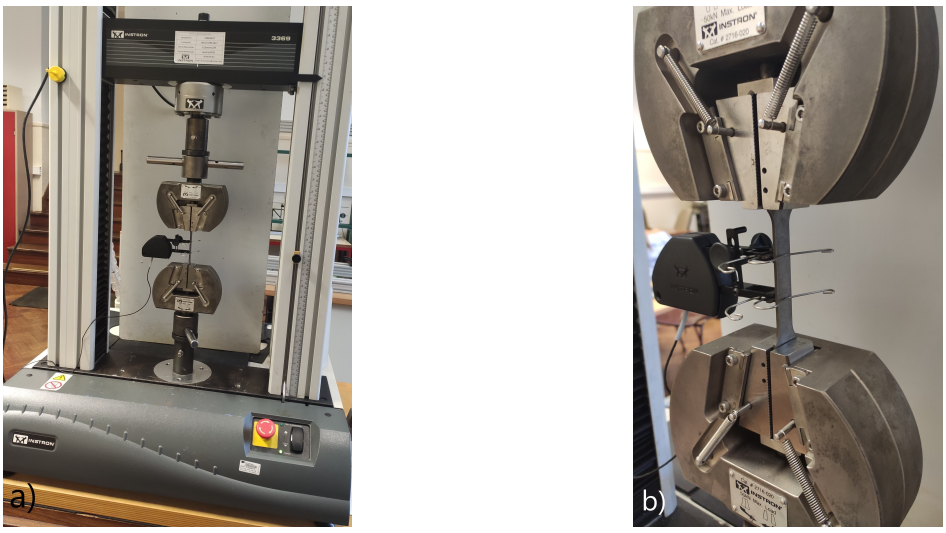

Figure 3.6: a) INSTRON® 3369; b) Specimen with a clip-gage.

3.6.1 Digital Image Correlation

As part of the tensile tests, a different strain measurement technique was performed by resorting to the Digital Image Correlation software or DIC. This method consists of a set of digital cameras that capture consecutive images of a specimen undergoing a mechanical test, in this case uniaxial tensile strength tests, and evaluate the change of its surface characteristics. The images taken are analysed by the software, which runs a mathematical correlation analysis.

For this method, a special preparation of the specimen is needed. A random pattern of points (speckle pattern) has to be created on the surface of the specimen, visible by the cameras. This process was made by painting the entire specimen with a white colour spray and then creating a random pattern with a black colour spray. Figure 3.8 shows a specimen with such pattern. After the specimen is painted, it is ready to be tested.

Before the test starts, 6 calibration images were taken, so the software can identify the initial position of the pattern. During the tensile test, the number of pictures taken was 2 per second for each specimen.

DIC tests were carried out at IST using the INSTRON® 3369 with 50 kN maximum load capacity, see Figure 3.6 a), and the cross-head speed was set to 1 mm/min, at room temperature. These parameters are the same as for the other tensile tests using a clip-gage. The software used to process the images was VIC-2D 2009 and the camera used was the Allied Vision Stingray F504B, see Figure 3.7.

Figure 3.7: Allied Vision Stingray F504B.

After the tensile test, data processing was needed. The software generated a strain map of the area of interest, selected by the user, where strains in the yy axis are shown and stress concentration areas can be distinguished.

3.7 Fatigue Tests

Fatigue performance is a crucial factor to take into account in the aerospace industry. It is then very important to study and understand the material's behaviour in such conditions.

In this work, the fatigue performance was assessed via the plot of an S-N curve. This method does not indicate the exact moment of crack formation but instead reveals the number of cycles until failure under certain load conditions.

Fatigue tests were carried out at IST in the INSTRON® 8502 machine, see Figure 3.9, at room

Figure 3.8: Specimen painted with a random pattern, ready for the DIC tensile test

temperature.

For all tests $R = \frac{\sigma_{min}}{\sigma_{max}} = 0.1$. These were ran until failure or if the run out criteria was reached, $N = 2$ x 10^6 cycles. Frequency of the loads was either 12 or 15 Hz, and maximum stress applied was kept between 450 and 550 MPa.

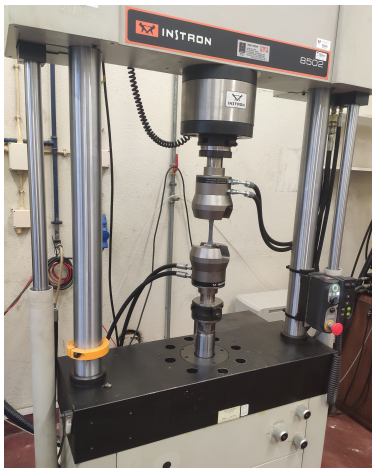

Figure 3.9: INSTRON® 8502.

3.8 Fractography Analysis

For the fractography analysis, using the Scanning Electron Microscope (SEM), small samples were cut from the fractured specimens of tensile and fatigue tests. The SEM has a focused beam of electrons, which interact with the specimen's atoms. These multiple interactions result in signals that contain information about the sample's composition and topography, which are then displayed in the computer [40]. SEM images were taken with magnifications from x500 up to x6000.

This analysis was focused on the fracture surface of the specimens in order to better understand the

type of fracture that occured and its characteristics and also detect possible material flaws.

This analysis was carried out at IST's MicroLab, at room temperature, and the microscope used for this analysis was the Analytical SEM Hitachi S2400, showed in Figure 3.10.

Figure 3.10: Analytical SEM Hitachi S2400, adapted from [40]

Chapter 4

Results

In this section, the results obtained from all studies performed are analysed and discussed. A comparison between specimens of the two different Heat input sets as well as between different wall locations will be recurrent. Some scientific publications are going to be cited to confirm the drawn explanations.

4.1 WAAM structures

Before entering in a more detailed analysis of the performance of the specimens for the tests carried out, attention should be paid to the differences between the obtained WAAM walls.

WAAM structures of both Heat input sets are presented in Figure 4.1. The front view does not evidence many distinctions between the two, but the side view confirms the disparity in width between them. The reason behind this phenomenon is attributed to the different travel speeds of each set, which influences the amount of material being deposited in each layer [24]. A lower travel speed, and consequently higher heat input, enables the deposition of more material, creating a slightly thicker wall.

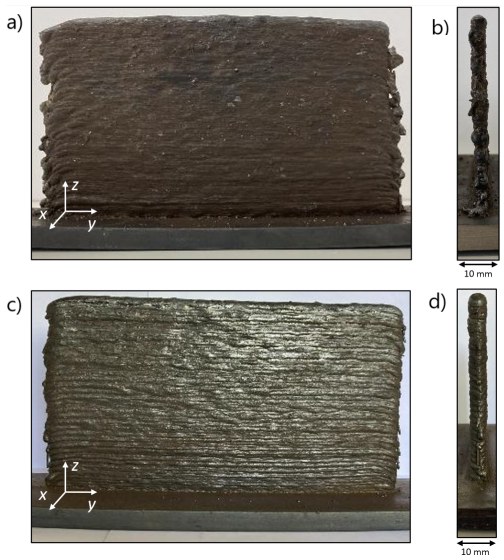

Figure 4.1: Wall structures manufactured with WAAM: Low Heat input: a) Front view; b) Side view; and High Heat input: c) Front view; d) Side view.

4.2 Hardness

Hardness was measured for samples in the base (a) and middle (b) positions, for LH and HH sets.

Both base and middle position samples exhibited a higher value of hardness for the LH input case. Such values are presented in the graph of Figure 4.2. Hardness is directly related to the homogeneity of the microstructure, so if the grains are more refined the sample will have higher hardness values. The HH input case favours grain growth, due to the high heat build up and lower cooling rate [24]. This means it is expected to have larger grains and lower values of hardness, which is in conformity with the results obtained.

To note that the heat build up and cooling rate also vary depending on the height of the wall. Material at the bottom of the wall is in contact with the substrate, meaning that the temperature gradient it experiences is higher. This is translated into a lower heat build up and a higher cooling rate. As the height increases, the heat build up increases and the cooling rate decreases.

In the results obtained, for the same heat input, base samples presented higher hardness than the middle ones, which can be verified in the graph of Figure 4.2. This goes in agreement with what was said in the previous paragraph.

The hardness values measured are thus in accordance with previous similar studies [24].

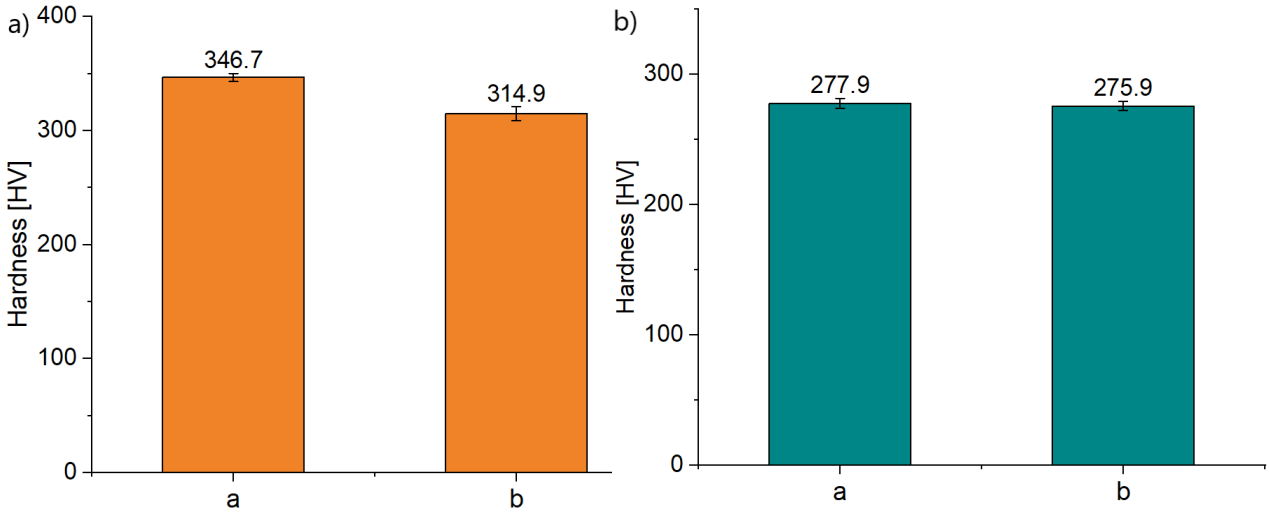

Figure 4.2: Hardness variation for each sample position for: a) Low Heat Input; and b) High Heat Input.

4.3 Microstructure observations

Following the hardness tests, microstructure observations were carried out for samples with base and middle locations, for LH and HH sets. For each sample, three surfaces were analysed, each one corresponding to a different direction. The scheme in Figure 4.3 illustrates this.

The microstructure of both walls, LH and HH, is represented in Figure 4.4, for face 2 of the samples.

In Figure 4.4, a clear difference between Low and High Heat input wall microstructures can be observed. Grain elongation is present for both cases, which is in agreement with literature reviews [18, 23].

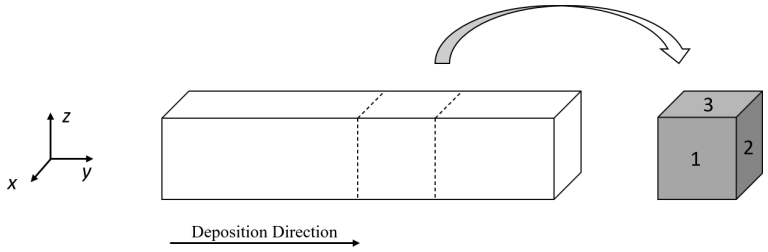

Figure 4.3: Scheme of the sample cut from a specimen (not at scale)

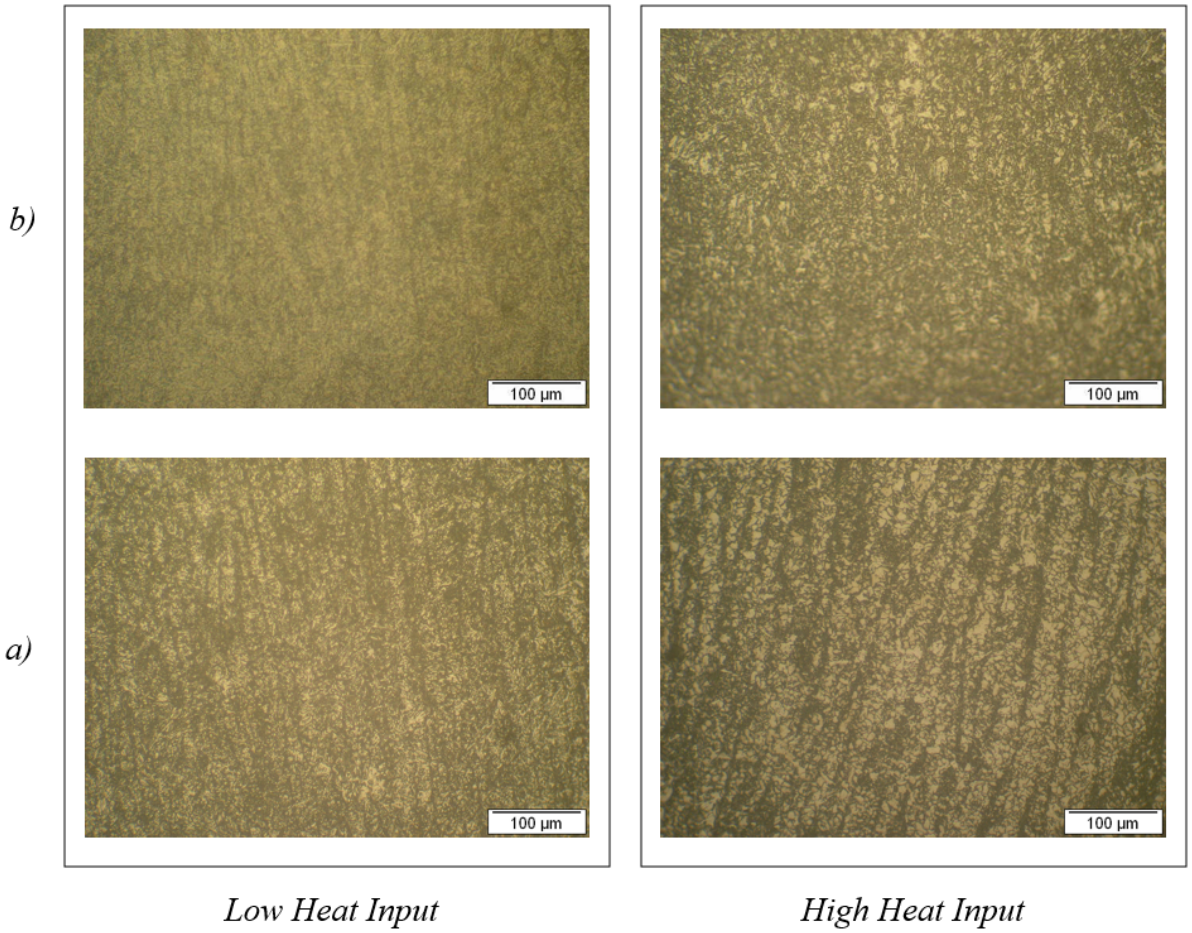

Figure 4.4: Microstructure (face 2): a) Base samples; b) Middle samples

Grain refinement in LH input is perceptibly higher than in HH input.

By observing the microstructure images, it is evident that an increase in heat input favours grain growth, as stated in chapter 2, as well as grain elongation. The reason behind the first statement is related to the increase in the heat build-up and lower cooling rates when the heat input is higher. This goes in compliance with what was mentioned in section 4.2.

Regarding grain elongation, and comparing both heat input sets, it was observed that lower temperatures felt during the deposition process were translated into a diminished temperature gradient and consequent attenuation of elongated grains formation.

The observations made also confirm the results obtained for the hardness. When heat input in-

creases, grains become larger and less refined, which leads to lower values of hardness.

Concerning the differences between base and middle samples, the observations made are only partly expected. As it can be witnessed, grain elongation becomes less perceptible as the height of the sample increases. This is explained by the decreasing temperature gradient felt by the deposited layers and happens to both Heat input sets, which is in compliance with previous similar works [24]. Regarding grain refinement, it is expected, according to literature and microhardness values obtained, to decrease as the height increases, however, it seems to be unclear whether or not grains belonging to the samples located in the middle of the structure, for both sets, are more or less refined than the ones located in the base samples. These observations do not allow a definitive conclusion about the characteristics of the material's microstructure along the wall's height. This issue might be solved by using a different reagent when contrasting the samples during their preparation, to better distinguish the grains boundaries.

This issue was also present in the images of the microstructure of face 3, which are also going to be presented, see Figure 4.5.

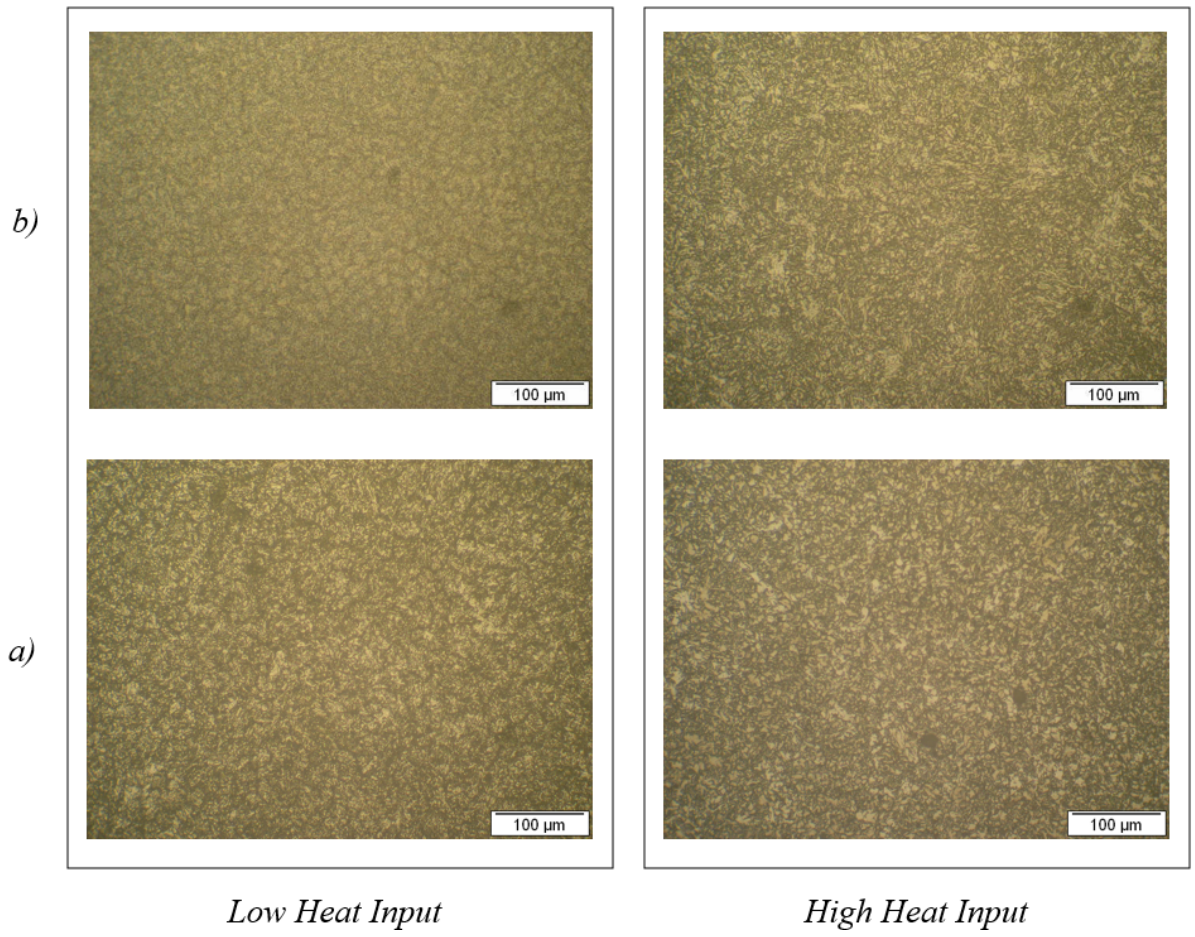

Figure 4.5: Microstructure (face 3): a) Base samples; b) Middle samples

After analysing Figure 4.5, it is clear that the tendency observed in the microstructure for face 2 is also present in face 3 of the samples, where grain growth is not perceptible by the images taken.

An important remark that must be made on face 3 is that it does not evince elongated grains. This is an anticipated behaviour because the temperature gradient, which is responsible for the elongation of

the grains, is acting in a direction normal to the plane of face 3 and not parallel like in face 2.

Lastly, for face 1, the structure's surface, particularly in the base location, suffered a rectification process during specimen fabrication, which may have caused a re-crystallization and consequent alteration of the microstructure. This helps to explain the lack of elongated grains in this part of the wall structure. Moving up to the middle location, for the same face, elongated grains are now observable. This can be confirmed in Figure 4.6. To note that the samples, 'a' and 'b', belonged to different walls, with the first one suffering the rectification process previously mentioned.

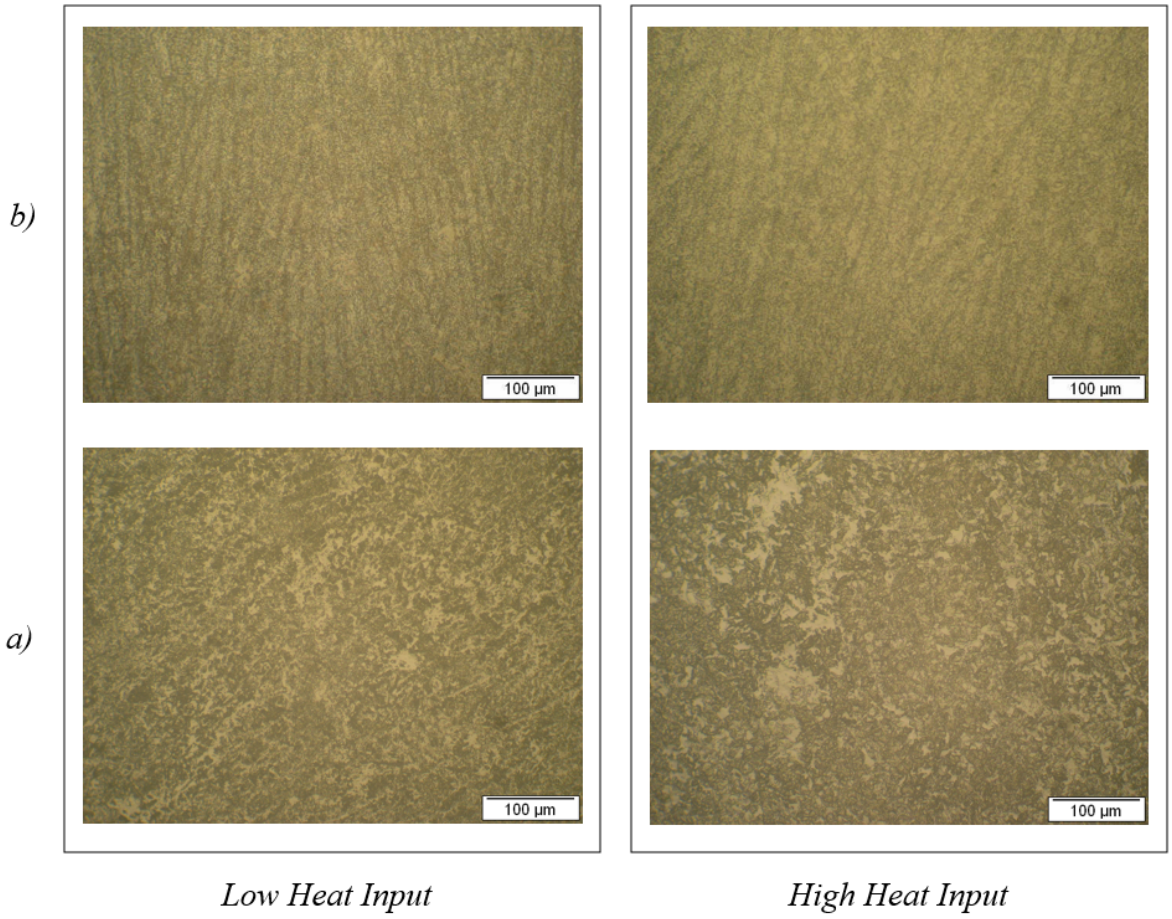

Figure 4.6: Microstructure (face 1): a) Base samples; b) Middle samples

Concerning isotropy, the wire material does in fact belong to this category, however, when choosing to use WAAM, the resultant deposited material does not present the same type of characteristics as the original.

It is clear, by comparing the images of the different sample surfaces, that the transformed material does not present an uniform microstructure, mainly due to the temperature gradient present during the layer deposition which contributed to formation of elongated grains and possible disparity in vertical and horizontal properties [14]. This characterization is out of the domain of this work.

Figures 4.7 show 3-D representations of a HH sample microstructure in the base and middle positions. Optically, the grain structure represented is clearly anisotropic. To note that these columnar grains can be detrimental for multi-axial loading conditions [20].

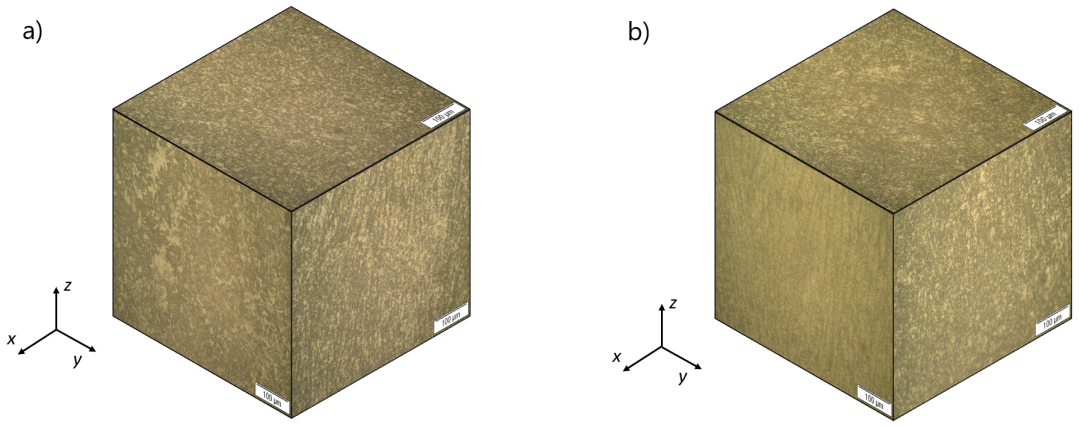

Figure 4.7: 3-D representation of the sample's microstructure: a) HH Base; b) HH Middle.

4.4 Tensile Tests

In this work, 18 specimens were subjected to tensile tests to evaluate their mechanical performance. Half of them corresponded to the LH input set and the other half to the HH input set. To note that both specimens tested with the usage of a clip-gage and DIC software were included in the presented results. Comparisons between heat input sets as well as between different specimen heights in the wall structure were made. All tests were carried out with a cross-head speed of 1 mm/min.

The wire material mechanical properties are presented in Table 3.2 and will serve as a reference to the ones measured in the WAAM specimens. It is expected, according to literature [13], deposited material properties to be significantly lower than the original ones.

After completing the tensile tests and tracing the Stress vs. Strain plot for each tested specimen, the most relevant properties were calculated and a few remarks can be pointed and discussed. It is also important to note that specimen 1La will not be included in the presented results due to its premature failure. This specimen displayed a large amount of surface irregularities, in particular 3 evident surface voids, which had major influence in its tensile performance, with failure occurring for a significantly lower displacement in comparison with the others. In section 4.4.5 a closer look at this specimen will be taken.

4.4.1 Elastic domain

The elastic domain will be analysed first. For this segment of the material behaviour there were no major deviations between specimens. Table 4.1 shows the mean values for each heat input set and Table 4.2 the mean value for each location, both for Young's modulus and resilience. The slight deviations in the elastic modulus results are caused by possible defects of the specimens (e.g. porosity) due to the deposition process.

Table 4.1: Mean values of E and Resilience for each heat input set.

	LH	HH
E [GPa]	196.5	204.6
Resilience [J/m^3]	1.65	1.67

Table 4.2: Mean value of E and Resilience for each height of each heat set.

	LH			HH		
	Base (a)	Middle (b)	Top (c)	Base (a)	Middle (b)	Top (c)
E [GPa]	203.8	195.3	192.8	204.9	200.9	208.1
Resilience [J/m^3]	1.89	1.82	1.31	1.62	1.82	1.57

In the calculations made, the value of yield strength was assumed to be the interception between the Stress vs. Strain curve of the specimen and a traced line starting at $\epsilon = 0.2\%$ with a slope equal to the Young's modulus of the specimen. Figure 4.8 shows two bar plots with the obtained mean values for this parameter.

No special trend can be spotted by observing the graphics of Figure 4.8, however, the values for c specimens tend to be lower than the other two heights, for both heat inputs. Although these differences are not significant, the results can reflect the slow vanishing of columnar grains in the wall microstructure, has the height increases, and the formation of equiaxed grains. These are related to an improve in ductility and consequent lowering of yield strength [20], which can explain the values obtained. To note that there were no disparities between heat input sets values, in what regards to yield strength.

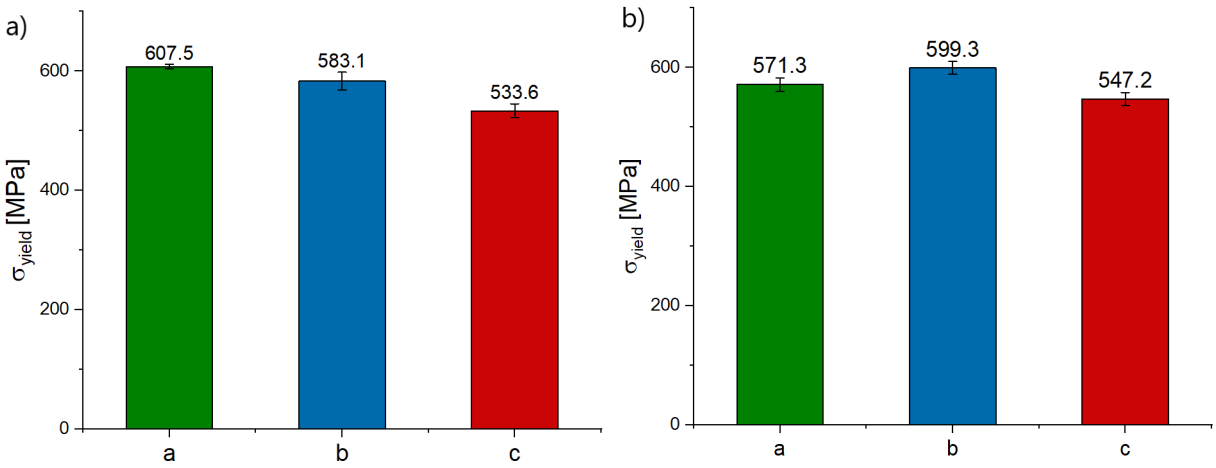

Figure 4.8: Bar plots representing yield strength values for a) Low Heat Input; and b) High Heat Input

When comparing this parameter mean value ($\sigma_{yield} = 571.7$ MPa) with the wire material ($\sigma_{yield} = 890$ MPa) there is a notorious difference. The most common solution to reduce this gap is to perform post-process heat treatment, that will alter the microstructure of the sample and improve its strength.

4.4.2 Ultimate Tensile Strength

Now focusing on the plastic domain, a few parameters were considered. Ultimate tensile strength (σ_U) for both heat input sets was calculated. In Figure 4.9 c) a visual comparison between the two is presented. It is clear that there is little to no difference between both sets, meaning heat input influence on ultimate tensile strength is not noticeable in these experiments. For the height, specimens 'a' present a slightly higher value than the other two, 'b' and 'c', see Figures 4.9 a) and b). Grain size, as well as of columnar grains, can have an important role in this matter. Grain increased refinement, as the height of the sample in the wall decreases, is usually responsible for the inflation of the UTS value, by means of

fine-grain strengthening mechanisms [23].

The values of ultimate tensile strength for the deposited material (LH: $\sigma_U = 908.7$ MPa ; HH: $\sigma_U = 912.4$ MPa) are very close to the wire's ($\sigma_U = 980$ MPa). Roughly 93% for both. This means that WAAM can successfully produce a structure without jeopardizing the maximum tensile strength supported by the feedstock material.

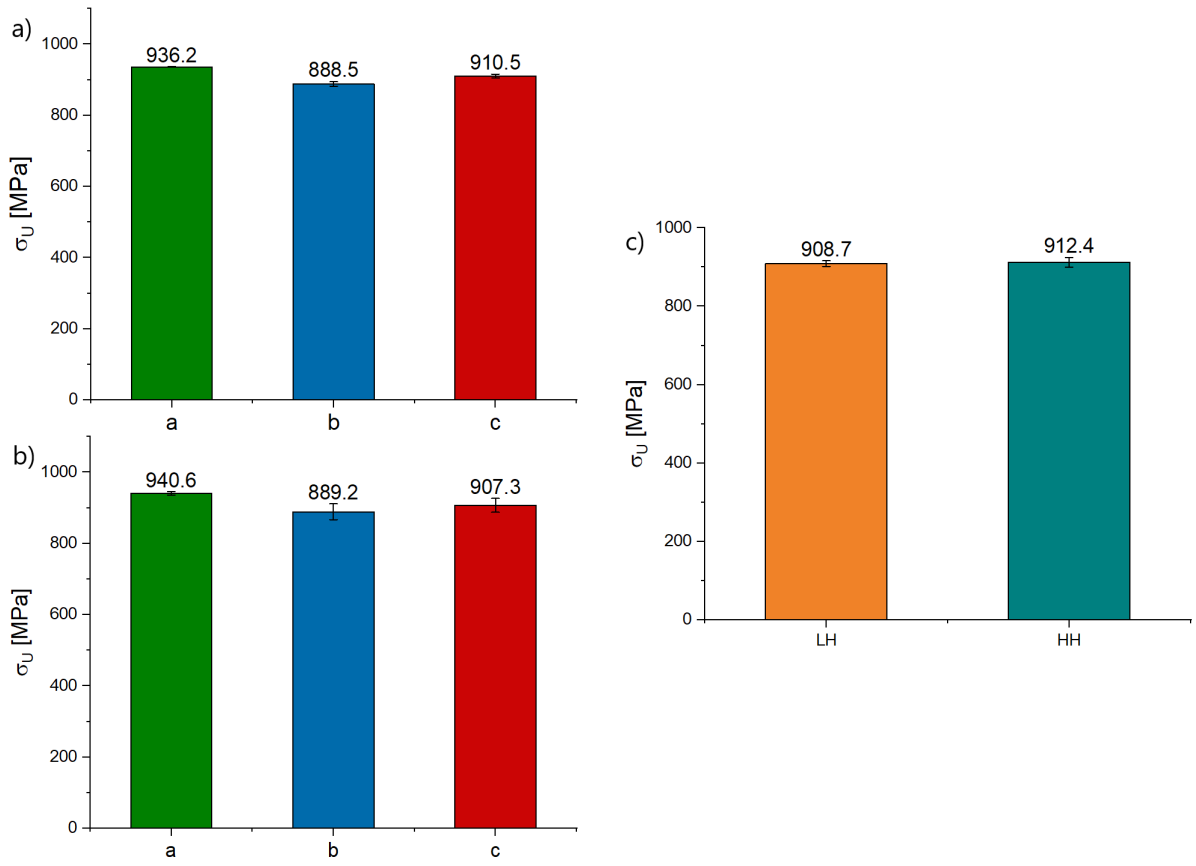

Figure 4.9: Bar plots representing σ_U values of each height for a) Low Heat Input; and b) High Heat Input. c) Bar plot representing σ_U values for each heat input set.

4.4.3 Maximum Strain

Regarding maximum strain attained by the specimens, results expose how microstructure differences can affect this parameter's value. Figure 4.10 shows the obtained values for each heat input set.

Analysing the plot in Figure 4.10, it is clear that Low Heat input specimens present a much higher value for maximum strain than High Heat input ones. These results are in accordance with literature and can be explained by the fine-grain strengthening mechanisms resultant from the superior grain refinement observed for the LH input set (section 4.3). This was caused by lower heat build up and higher cooling rates in comparison with the HH input set, as already explained in section 4.2.

As for the different heights, odd results were obtained, with the maximum strain increasing with height for the LH input set, see Figure 4.11 a), and having a non systematic behaviour for the HH input set, see Figure 4.11 b). Also, to note that the standard error registered for each bar was significant, making it hard to formulate assertive comments on this topic. According to the observations made on the specimens

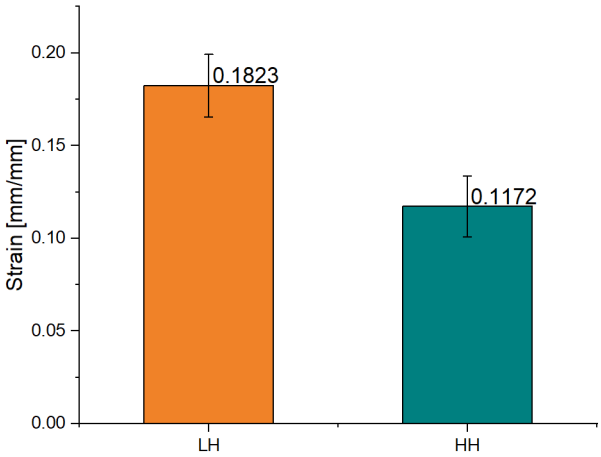

Figure 4.10: Bar plot representing maximum strain values for each heat input set.

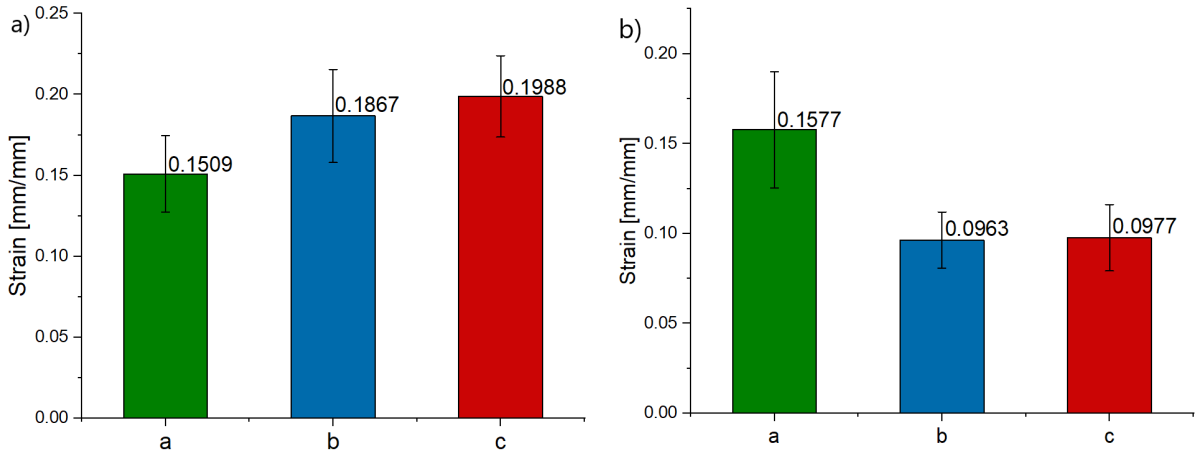

Figure 4.11: Bar plot representing maximum strain values for each height: a) for the LH input set; and for the HH input set.

microstructures, where grain growth is not noticeable from the base to middle locations, maximum strain should also not be affected and maintain similar values for the different heights. This leads to believe that the issue might be related to an experimental error, for example the strain measurement technique, or even material flaws.

4.4.3.1 DIC measured Maximum strain

To investigate the odd results obtained for maximum strain for all specimens, the ones whose strain was measured using DIC, considered to be more accurate than the clip-gage, were isolated from the others and their results analysed. This included specimens: 1Lb; 1Lc; 4Ha; 4Hb; and 4Hc.

When analysing the graphs in Figure 4.12, the maximum strain results along the wall structure are very different from the previously analysed ones. Here, they are kept relatively constant, meaning sample's height does not affect its maximum strain, which is in accordance with the observations made on the material's microstructure and grain growth along the wall. For the LH input set, there is a general increase in the values for each specimen location, however, it was not possible to evaluate location 'a' value as specimen 1La, which was also tested using DIC, failed earlier than expected and did not

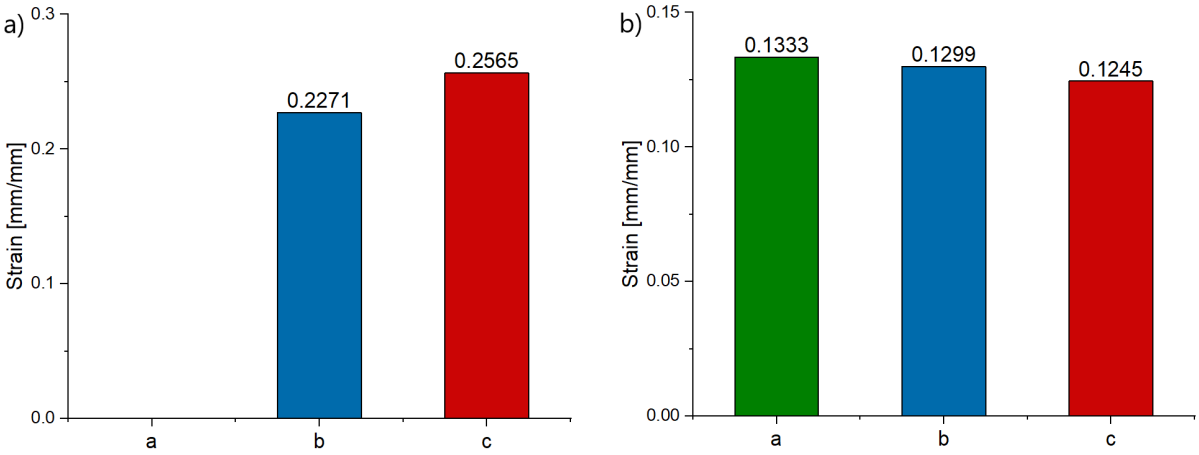

Figure 4.12: Bar plot representing maximum strain values for each height for specimens tested with DIC: a) for the LH input set; and for the HH input set.

present valuable results. Regarding the HH input set, a drastic change can be spotted. Similar and higher values were obtained for all specimen locations, which is according to the expected.

As for the comparison between heat input sets, the trend is maintained with the LH input set having higher values of maximum strain than the HH input set, see Figure 4.13.

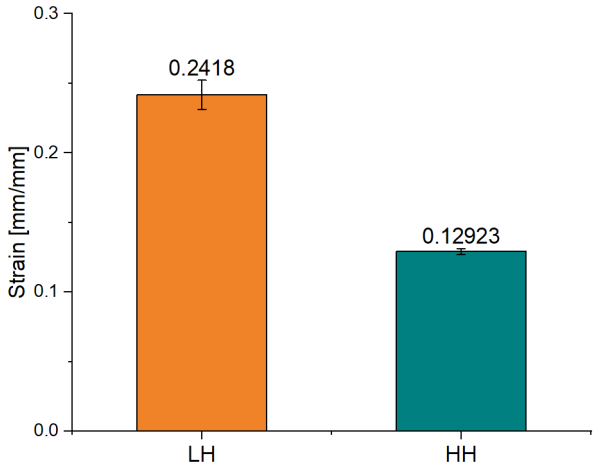

Figure 4.13: Bar plot representing maximum strain values for each heat input set, for specimens tested with DIC.

DIC tensile tests helped prove that possible experimental errors, associated with the strain measuring technique, happened during the tensile trials that used a clip-gage to measure this parameter.

This device, despite being of easy usage, presented some setbacks that could have influenced the obtained results. The fact that it 'grabs' the specimen and is in direct contact with it can affect its stress distribution and alter the resultant values. Also, in many cases, the specimen's failure did not occur in the area measured by this device, which can lead to strain measurements different that reality. Figure 4.14 shows three specimens that failed outside the blue lines delimiting the clip-gage measuring area.

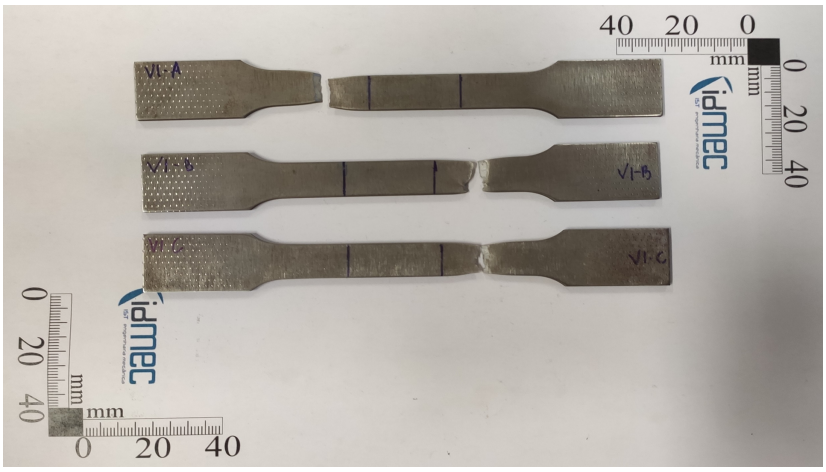

Figure 4.14: Three specimens in which failure occurred outside the clip-gage measuring area.

4.4.4 Toughness

Material toughness is related to the ability to absorb energy and plastically deform without fracturing. This parameter is obtained by calculating the area under the Stress vs. Strain curve of each specimen. Figure 4.15 shows three graphs with the summarized results for each heat input and each height.

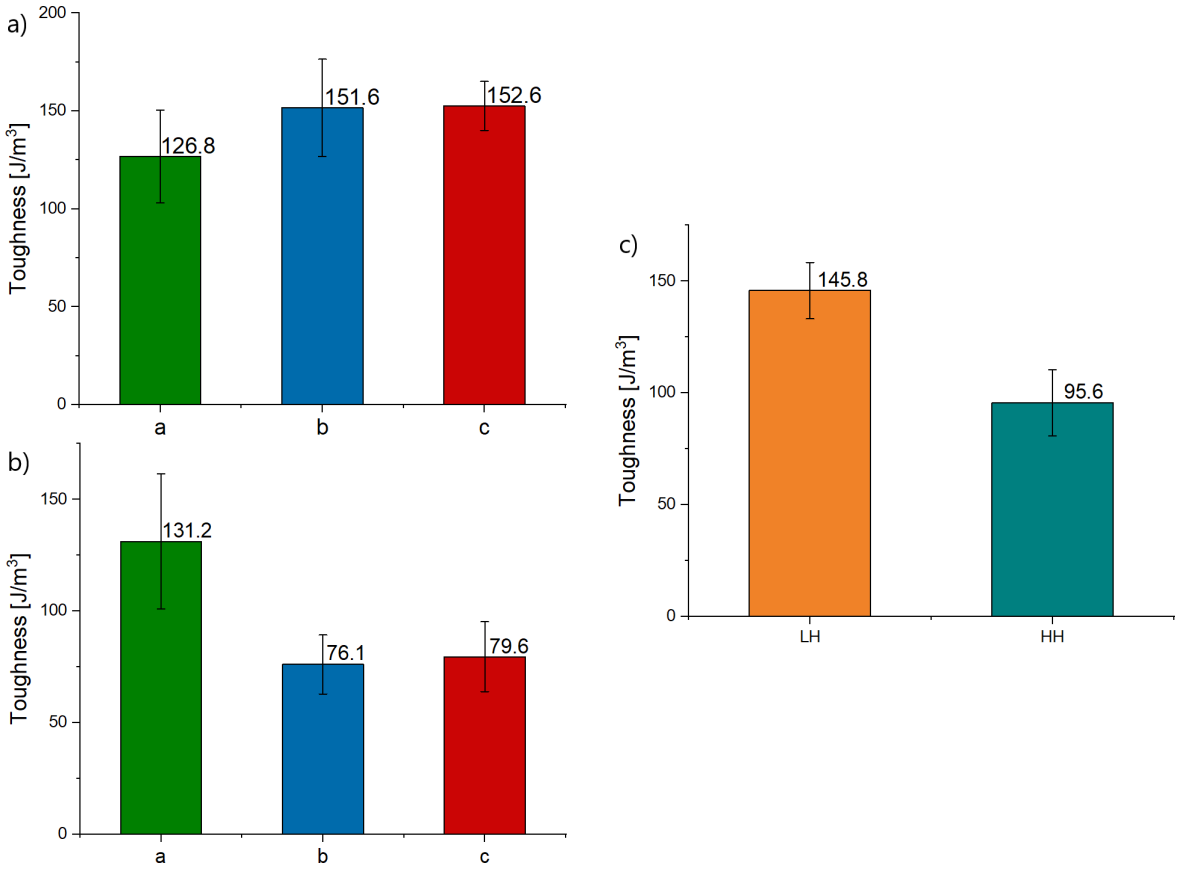

Figure 4.15: Bar plots representing toughness values of each height for a) Low Heat Input; and b) High Heat Input. c) Bar plot representing toughness values for each heat input set.

It is interesting to note that this parameter has a similar behaviour to the maximum strain. The reason

behind it is that the area under the curve depends on both UTS and maximum strain, and since the first one does not evidence major differences between heat input sets or specimen heights, toughness variation will be mainly connected with maximum strain.

4.4.4.1 DIC measured Toughness

In a similar way to maximum strain, toughness was also calculated only with the specimens tested via DIC. Results follow the same trend as maximum strain, see Figure 4.12, as expected. Figure 4.16 presents the graphs with those values.

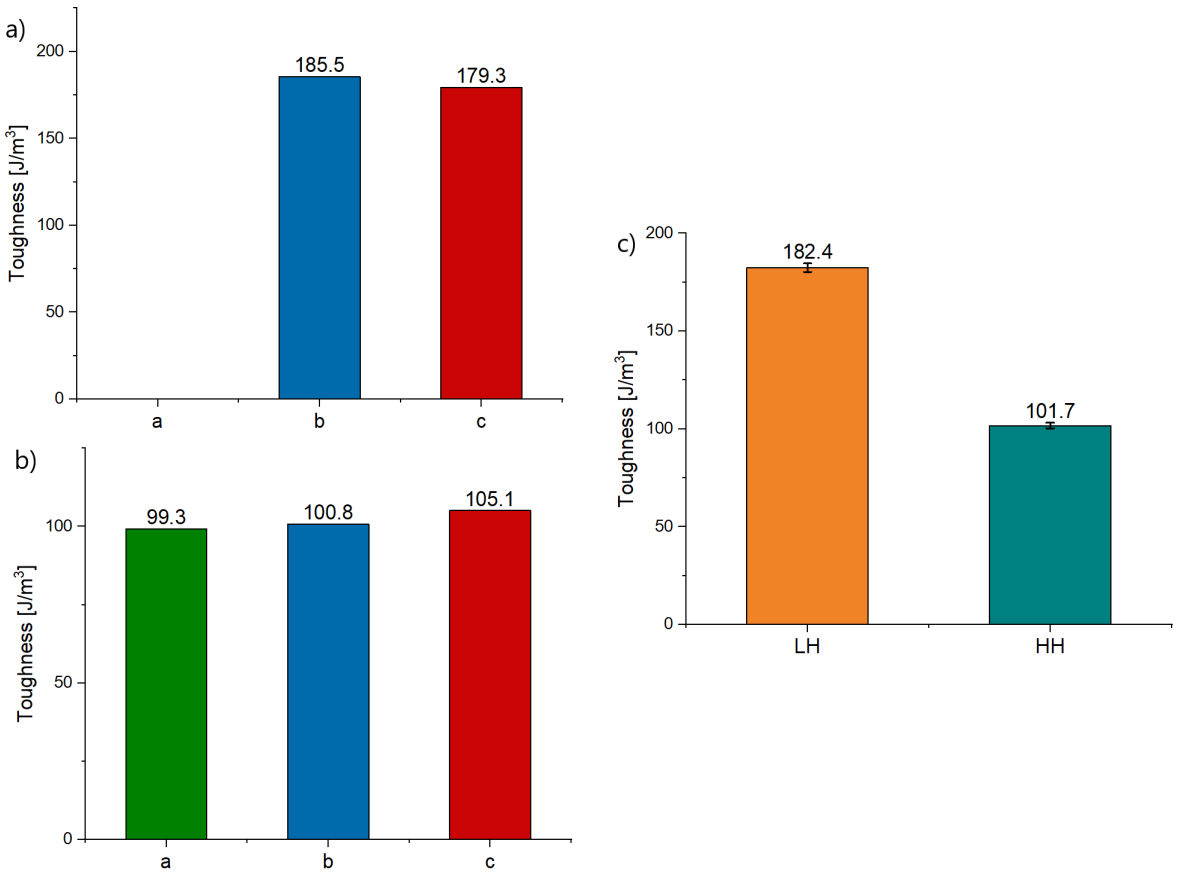

Figure 4.16: Bar plots representing toughness values of each height for a) Low Heat Input; and b) High Heat Input. c) Bar plot representing toughness values for each heat input set.

4.4.5 Specimen 1La

In the previous sections, results of tensile tests performed with DIC were presented and discussed. It is however important to note that specimen 1La was not included in the results. This specimen suffered approximately 1/3 of the deformation to break, in comparison to the others of the same category, due to a large amount of surface irregularities, in particular 3 evident surface voids.

Figure 4.17 a) shows a picture of the specimen in question and the three surface voids marked with red circles. In Figures 4.17 b) c) and d), the evolution of stress distribution in the material's surface is presented. To note that the painted surface, displayed in this image chain, is in the back of the one

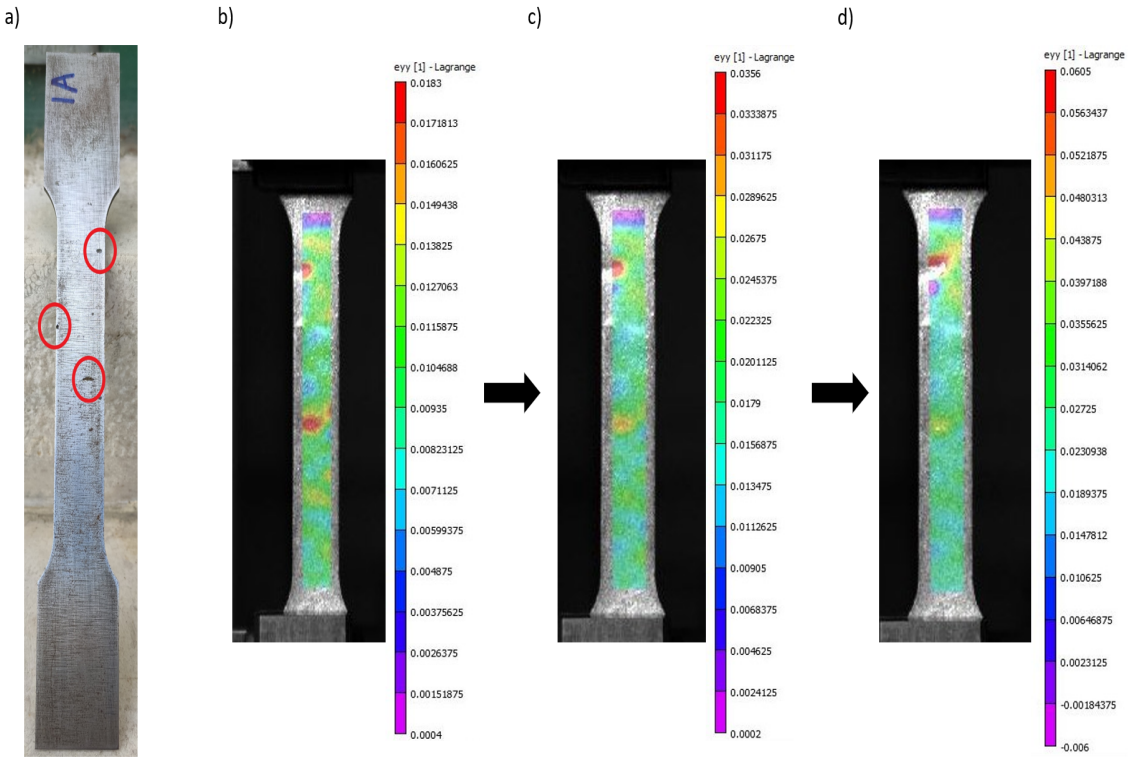

Figure 4.17: a) Specimen 1La with significant voids identified; Strain distribution along the surface of specimen 1La when: b) displacement equal to 1.594 mm; c) displacement equal to 2.273 mm; d) failure occurs.

represented in Figure 4.17 a), so the concentration zones are expected to develop in a mirrored location, as will be demonstrated. This also happens to all other specimens tested with DIC.

When analysing the pictures of Figure 4.17, it becomes clear that the voids detected prior to the tensile loading are in fact the main causes of stress concentration in the specimen. Figure 4.17 b) shows two points of high stress concentration, corresponding to two void locations. The third one, however, is evidently not present. This is because it is located on the edge of the specimen's surface which is not included in the software's area of interest. Nevertheless, stress distribution evolves into a single stress concentration area, Figure 4.17 c), which ultimately leads to failure of the sample, Figure 4.17 d).

4.4.6 Specimen 4Hc

Prior to subjecting specimen 4Hc to a tensile loading test, a void was identified in its surface and special attention was taken to it. Figure 4.18 a) presents the location of such imperfection.

Since this specimen was tested using the DIC method, the strain distribution along its surface was followed and the influence of the void analysed.

In Figure 4.18 b), strain values are evidently higher around the area where the surface imperfection is located. Strain distribution evolves, see Figure 4.18 c), and stresses start to concentrate solely on the void's location. Material rupturing is also beginning to get noticed on that spot. This is then followed by the failure of the specimen, see Figure 4.18 d). The visual analysis provided by DIC software demonstrates the influence that an imperfection can have in the behaviour of a specimen during tensile

loading.

Despite being a clear stress raiser, the presence of a void did not significantly affect the tensile properties of specimen 4Hc, when compared to specimen 1La. This latter, however, presented more than one surface imperfection which highly contributed to its poor tensile performance.

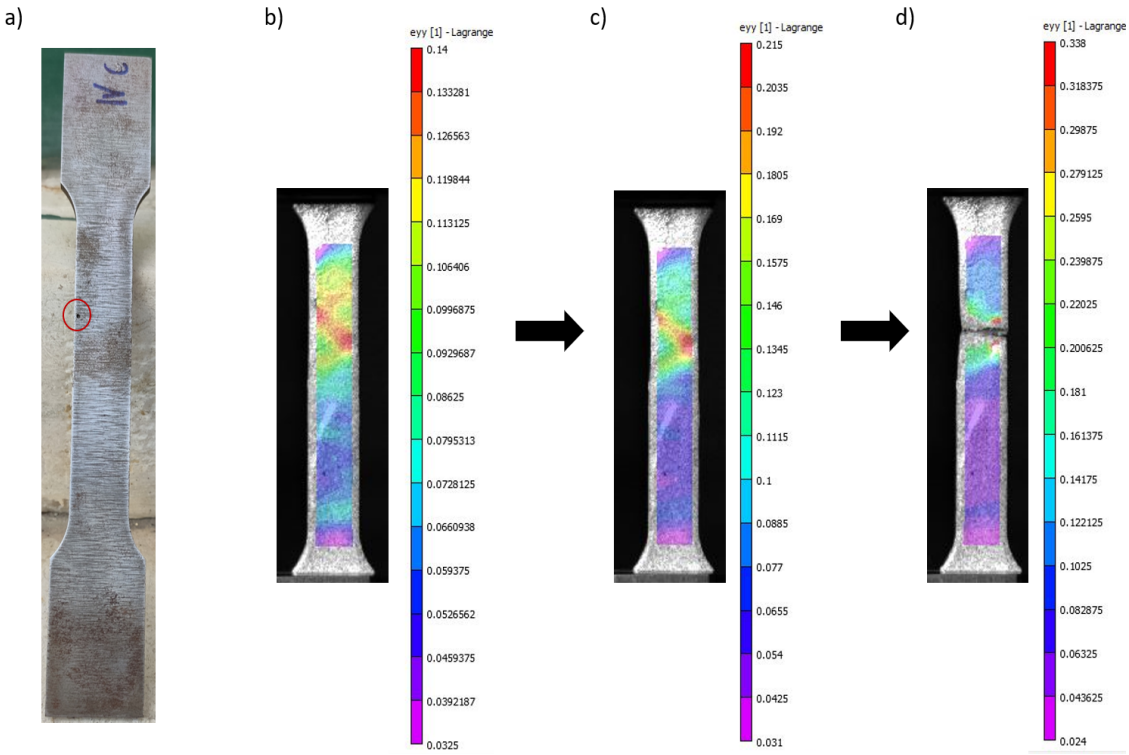

Figure 4.18: a) Specimen 4Hc with identified void; Strain distribution along the surface of specimen 4Hc when: b) displacement equal to 7.658 mm; c) displacement equal to 8.091 mm; d) failure occurs.

Overall, DIC results were found to be more accurate than the clip-gage ones primarily due to the possibility of choosing were to place the software created extensometer. When knowing, beforehand, where the given specimen would fail, it became easier to make sure that in fact the correct strain was being measured. Figure 4.19 shows a software created extensometer applied to specimen 4Hc in the area of most interest.

4.5 Fatigue Tests

In the aerospace industry fatigue performance of aircraft structures is of paramount importance. WAAM manufactured specimens were subjected to a cyclic loading to access their fatigue life and the results were interpreted via an S-N curve. Table 4.7 shows the parameters chosen for each tested specimen as well as their results. To note that these trials were performed under load control and therefore belong to the High Cycle Fatigue (HCF) category.

$$S = -13.44log(N) + 693.6, \quad R^2 = 0.0905 \tag{4.1}$$

Equation 4.1 demonstrates the trendline approximation for the obtained values of the specimens that

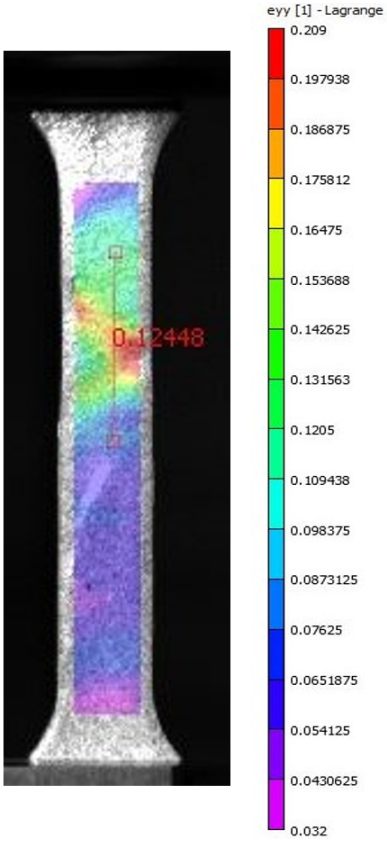

Figure 4.19: Software created extensometer applied to specimen 4Hc.

Table 4.3: Fatigue tests parameters and results.

Specimen	Max. Stress [MPa]	Max. Load [N]	Min. Load [N]	Load Amp. [N]	Freq. [Hz]	Cycles to failure
8La	450	14850	8167.5	3341.25	15	Runout
8Lb	550	18150	9982	4084	12	92771
8Lc	525	13230	7276	2977	12	97851
9La	550	13920	7656	3132	12	73300
9Lb	500	12600	6930	2835	15	Runout
9Lc	525	13119	7216	2951.5	12	112126
10La	510	16830	9256.5	3786.75	12	Runout
10Lb	525	17325	9528.7	3898.15	12	160099
10Lc	550	18150	9982	4084	12	155881

failed before the 2 x 10^6 cycles run out criteria. S stands for the maximum stress applied and N the number of cycles until failure. With an $R^2 = 0.0905$ it is clear that this approximation does not represent the true behaviour of the material.

During fatigue testing, an unexpected occurrence took place as the specimens which were subjected to a maximum stress ≤ 510 MPa did not fail during the tests and reached the run out criteria while the ones subjected to a maximum stress ≥ 525 MPa failed much earlier than 2 x 10^6 cycles, the maximum being 160099 cycles to failure for specimen 10Lb.

The explanations for this happening are not very clear. In literature, pre-straining of the material was found to induce considerable hardening and led to a significant discrepancy on fatigue life results. Major microstructural modifications were identified and described as secondary hardening, for HCF. This was

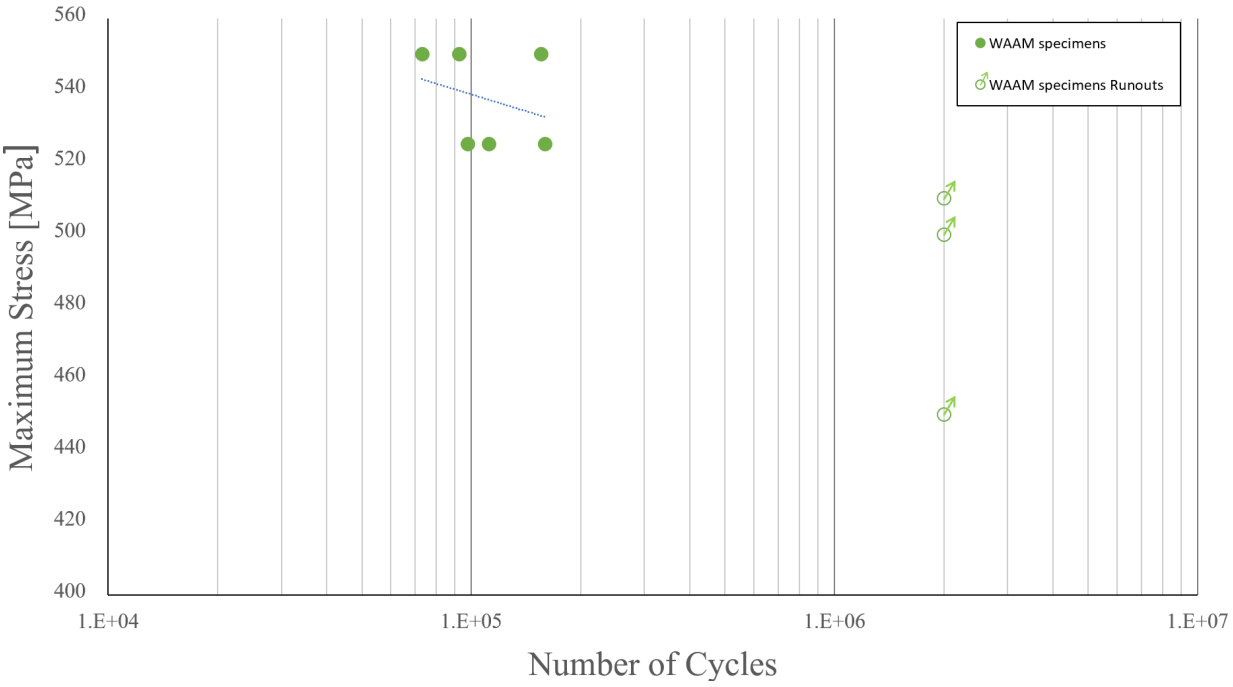

Figure 4.20: S-N curve of the tested WAAM specimens.

characterized by a significant cyclic hardening as well as extension of specimen fatigue life [41].

Different studies, not specifically about WAAM materials, using Low Cycle Fatigue and therefore being strain controlled tests, observed that in fact a secondary hardening, or secondary softening, phenomenon occured primarily due to certain strain amplitudes [42, 43]. The assessment of whether or not this is happening in the specimens tested stays out of scope of this dissertation and should be analysed in future works.

4.6 Fractography Analysis

In addition to to the experimental tests and microstructural analysis carried out, a detailed look upon the fracture surface of the specimens should be performed. After the tensile and fatigue tests were finished, the most relevant specimens were chosen to be observed in the SEM, see Table 4.4.

Table 4.4: Specimens to be observed in the SEM.

From Tensile Tests	2La	5Hc				
From Fatigue Tests	8Lb	8Lc	9La	9Lc	10Lb	10Lc

Little differences can be spotted between the images of Figure 4.21. Specimen 2La (Low Heat input) presents a slightly more refined microstructure with smaller grain size than 5Hc (High Heat input). This goes in accordance with what was also observed in section 4.3, regarding different heat input sets.

When analysing specimen 10Lc, important observations were made on the material's fracture mode. By looking at Figures 4.22 a) and b), taken in the middle of the fracture surface, there is a clear presence

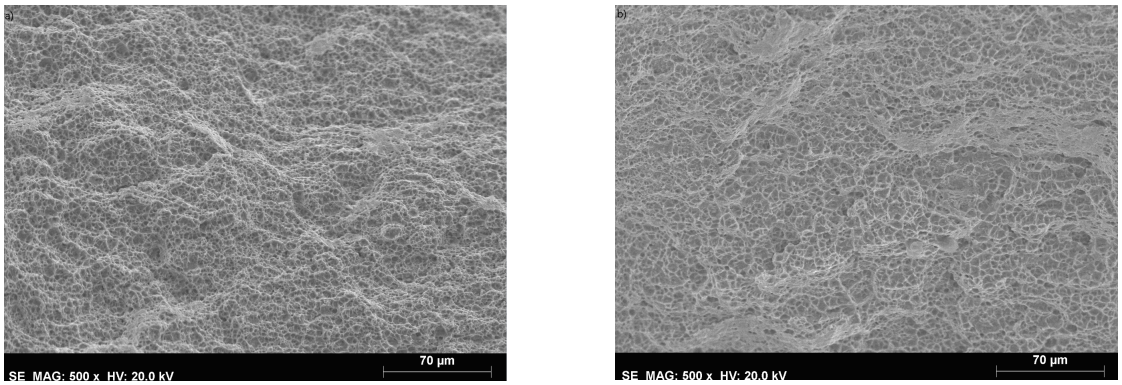

Figure 4.21: Detailed view along specimen surface and under an amplification of x500 : a) specimen 2La; b) specimen 5Hc.

of striations, indicating that the specimen suffered a ductile fracture [44]. At the edge of the fracture surface, a secondary cracking occurs. Here, striations are also present, see Figures 4.22 c) and d), showing again the ductility of the material. Naked-eye observations of the specimens' fracture surface are in accordance with these. Lastly, Figures 4.22 e) and f) were taken far from the fracture surface. Running a quick analysis, a few black dots are noticeable. These are thought to be microvoids resultant from the pullout of the grains. This is seen as a sign of an unstable failure of this part of the specimen.

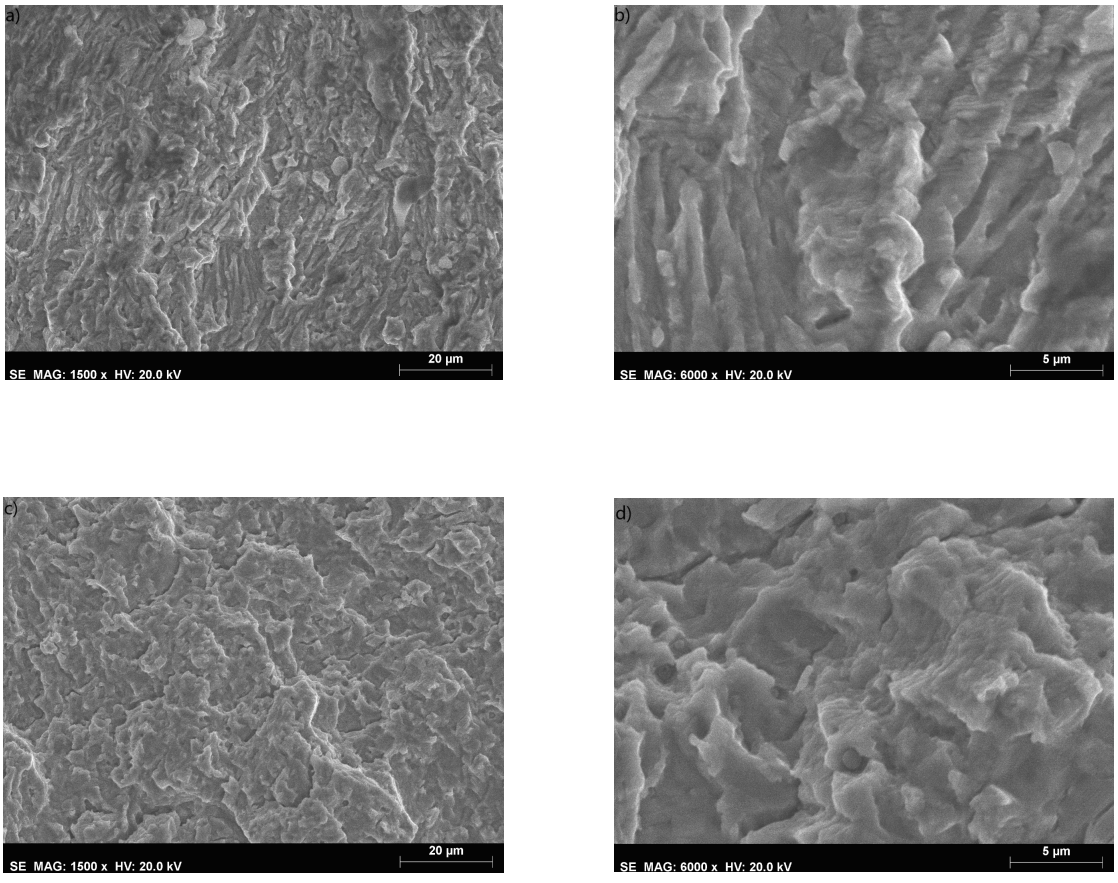

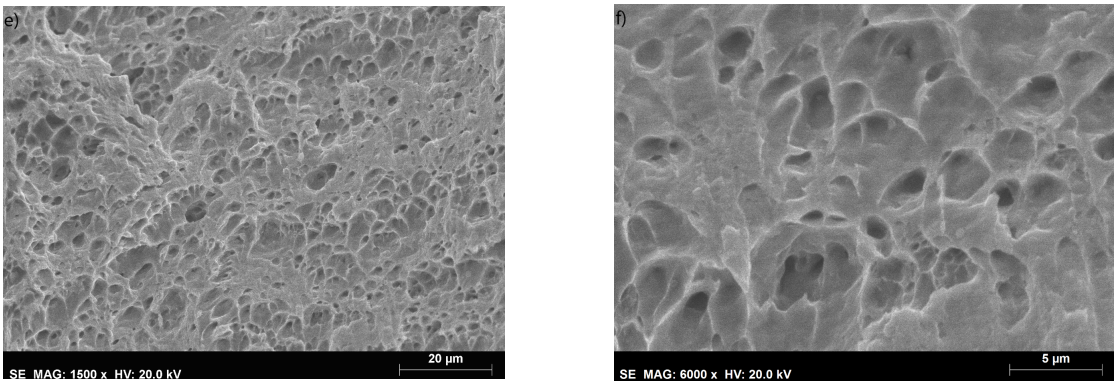

Figure 4.22: Detailed view of: specimen 10Lc microstructure at the primary fracture surface under an amplification of a) x1500; and b) x6000; specimen 10Lc microstructure at the secondary fracture surface under an amplification of c) x1500; and d) x6000; specimen 10Lc microstructure outside the fracture surface under an amplification of e) x1500; and f) x6000.

Figure 4.23 shows the chemical composition of sample 9Lc calculated with SEM. Apart from the lack of Mo (0.5%), there are no unusual observations. The same analysis was performed on other specimens with similar results.

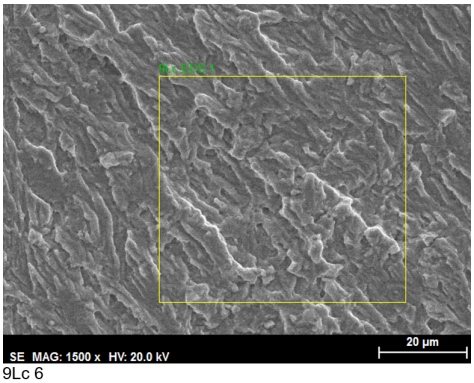

9Lc 6
Date:28-10-2020 11:32:06
Image size:2000 x 1500
Mag:1500x
HV:20.0kV

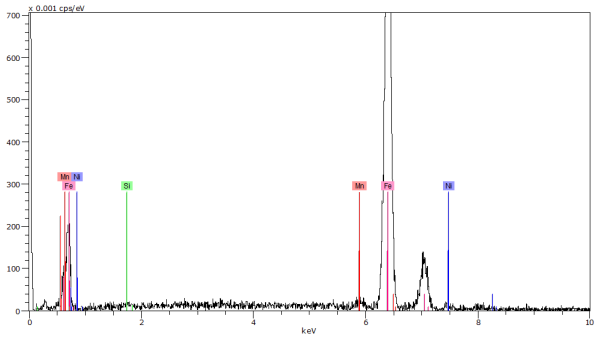

9Lc EDS 1.spx Date:28-10-2020 11:32:30 HV:20.0kV Puls th.:0.48kcps

El	AN	Series	unn. C [wt.%]	norm. C [wt.%]	Atom. C [at.%]	Error (1 Sigma) [wt.%]
Fe	26	K-series	211.48	97.58	97.47	6.07
Mn	25	K-series	2.79	1.29	1.31	0.26
Ni	28	K-series	2.13	0.98	0.93	0.29
Si	14	K-series	0.32	0.15	0.29	0.09
		Total:	216.72	100.00	100.00	

Figure 4.23: Analysis of the specimen 9Lc chemical composition.

Chapter 5

Finite element analysis

To better understand how accurate the work done in this dissertation was, it is beneficial to build FEM models representing the tests performed. The comparison between numerical and experimental results will help determine the efficiency of the work done and ultimately aid in the prediction of the joint's performance in its service life.

FEM consists on the division of the specimen into various finite elements. Due to an increased computational effort required by fatigue studies, the simulations were only performed for tensile tests, with the determination of the strain distribution as well as the Stress vs. Strain curve, only until ultimate tensile strength was reached.

To perform the finite element modeling, the utilized software was Siemens NX.

5.1 Specimen modeling

In order to successfully simulate the tensile behaviour of the specimens, both elastic and plastic domains should be considered. For this, a structural analysis using *SOL 401 Multi-Step Nonlinear* with *Simcenter Nastran* solver was chosen. This simulation required the Young's modulus, Poisson's ratio and the values of the Stress vs. Strain curve of the material. Given that the Poisson ratio was not calculated during the experiments, it was assumed to be approximately $\nu = 0.3$, for steels [45]. Both the elastic modulus and the values of the Stress vs. Strain curve were changed according to the specimen being simulated. To note that the simulation only included part of the stress curve, until the ultimate tensile strength was reached.

5.1.1 Mesh

The specimens were designed in Siemens NX software, according to their dimensions, and a 3D mesh was applied to them with an element size of 1 mm. This decision was based on a mesh convergence study, presented in section 5.1.1.1. All models consisted on CHEXA(20) elements, a 20-node three-dimensional element illustrated in Figure 5.1. Figure 5.2 presents a specimen with the applied mesh.

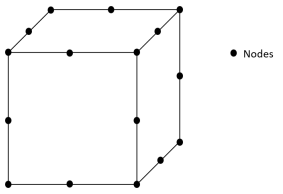

Figure 5.1: CHEXA element used in the FE analysis.

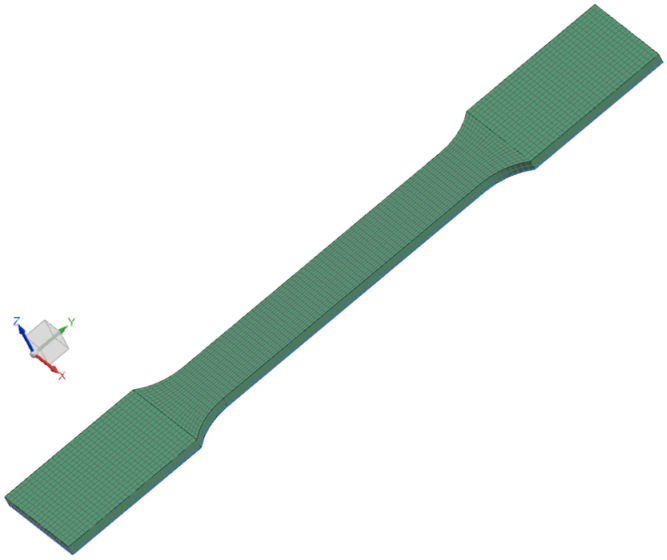

Figure 5.2: Specimen FE 3D mesh.

5.1.1.1 Mesh Convergence Study

In order to find the best conjugation between the level of refinement of the applied mesh and the computation time taken, a convergence study must be carried out. For this, the maximum stress recorded during the simulations for specimen 6Ha was the output result to be analysed. Six different meshes were created, with increased refinement, from 5 to 0.5 mm of element size. Table 5.1 presents the characteristics of each one and the resultant information from the simulations.

Table 5.1: Mesh convergence results.

Mesh	Element Size [mm]	Nº of elements	CPU Time [s]	Maximum Stress [MPa]	|Error| [%]
1	5	100	10.03	1128.06	1.209424
2	2	562	15.61	1117.24	0.238655
3	1.5	991	25.78	1116.27	0.151627
4	1	4556	323.46	1114.42	0.01436
5	0.7	13884	954.23	1114.76	0.01615
6	0.5	35640	2202.25	1114.58	-

The error percentage was calculated with respect to mesh 6, given that it had the greater refinement and therefore the most accurate value of maximum stress. Analysing the results, the last two meshes (4 and 5) showed a significantly lower error percentage, $< 0.10\%$, when compared to the others and therefore presented themselves, along with mesh 6, to be the preferable choices. As for the CPU time,

mesh 4 has a significantly lower value when compared to meshes 5 and 6. Taking these into account, and with the aim of keeping a low computational time without jeopardizing the accuracy of the results, mesh 4, with an element size of 1 mm, was the chosen mesh to be applied to the simulated models.

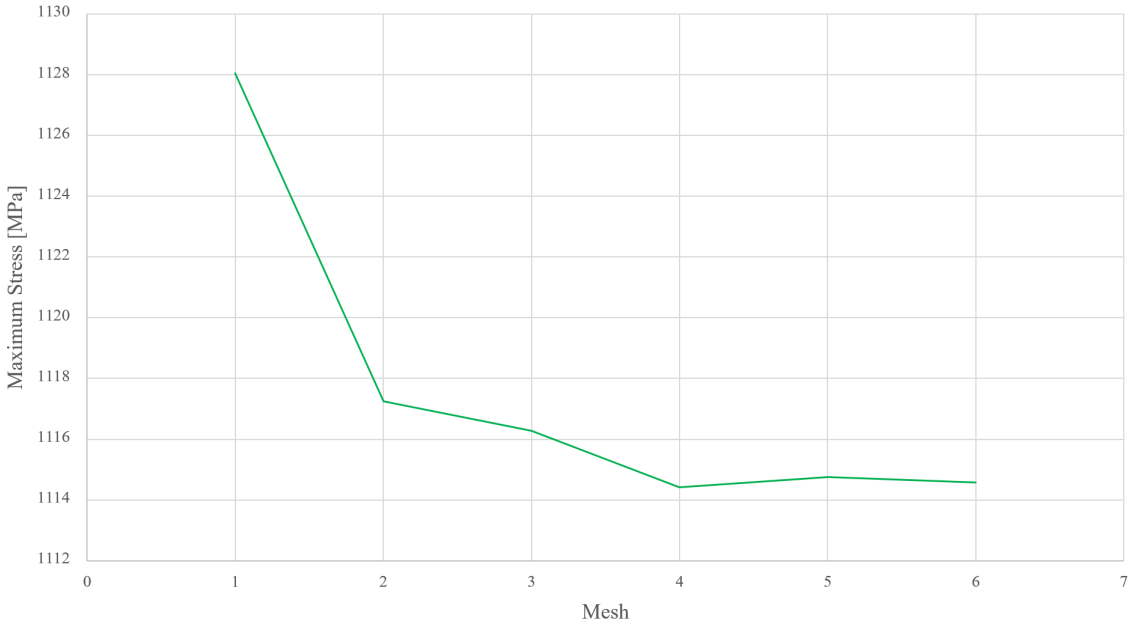

Figure 5.3: Graphical representation of Mesh convergence results.

Figure 5.3 shows a graphical representation of the convergence results.

5.1.2 Boundary conditions

The numerical models constructed tried to emulate, as close as possible, the real experiment parameters. The tensile tests performed were strain controlled, with a cross-head speed of 1 mm/min. To replicate this, a transient simulation would be necessary, taking a lot of time and computational effort. Since the finite element modeling is only a complementary aspect of this dissertation, it was decided to adopt a static approach.

A fixed constraint (encastrated) was applied to the bottom of the specimen and an enforced motion, in the yy direction, to the top of the specimen, see Figure 5.4.

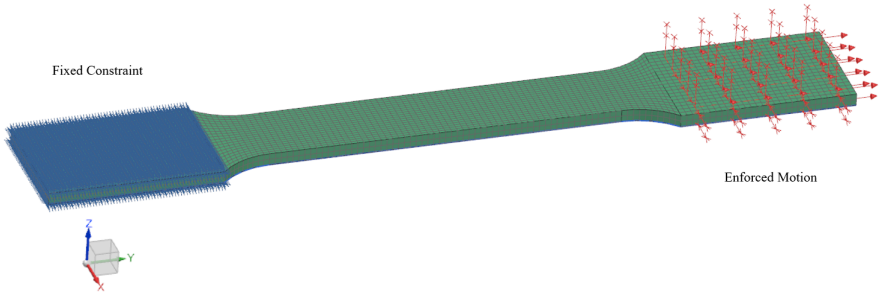

Figure 5.4: Boundary conditions on the simulated specimen.

5.2 Numerical results

Numerical simulations were performed on two different specimens, 1Lc and 6Ha. One for each strain measurement technique, with DIC (1Lc) and with clip-gage (6Ha). The overall results were fairly satisfactory, with the experimental behaviour of the specimens having a decent approximation to the finite element modeling.

5.2.1 Tensile Test - 6Ha

The stress distribution of specimen 6Ha is represented in Figure 5.5. The area with the highest stress is distributed along the the middle of the part.

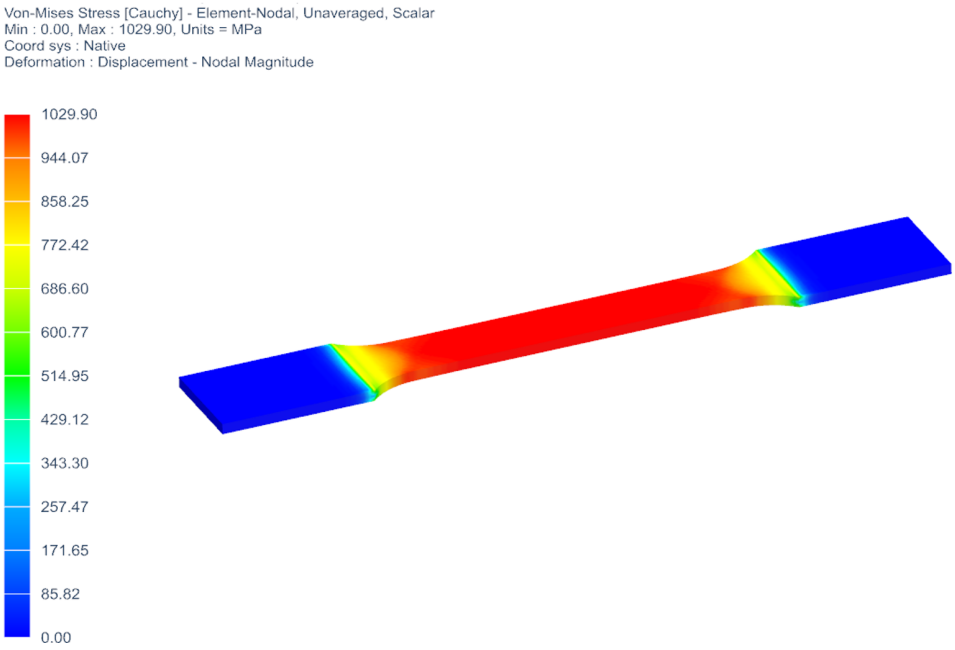

Figure 5.5: Siemens NX 6Ha specimen stress model, in the plastic domain.

Figure 5.6 shows a chart with a comparison between experimental and numerical results for this specimen.

By analysing Figure 5.6, it is fair to assume that both results are similar to each other. To note, however, that the numerical line extends to higher strain and stress than the experimental. The explanation for this small discrepancy might be associated with surface irregularities or porosity present in the specimen or slightly incorrect strain measurements by the clip-gage.

5.2.2 Tensile test - 1Lc

The strain distribution of specimen 1Lc, obtained from the FEM model is represented in Figure 5.7 a).

Since this specimen was tested using DIC, the comparison between the numerical and experimental strain distribution can also be made visually. Figure 5.7 b) shows the strain distribution, processed via VIC 2009 software.

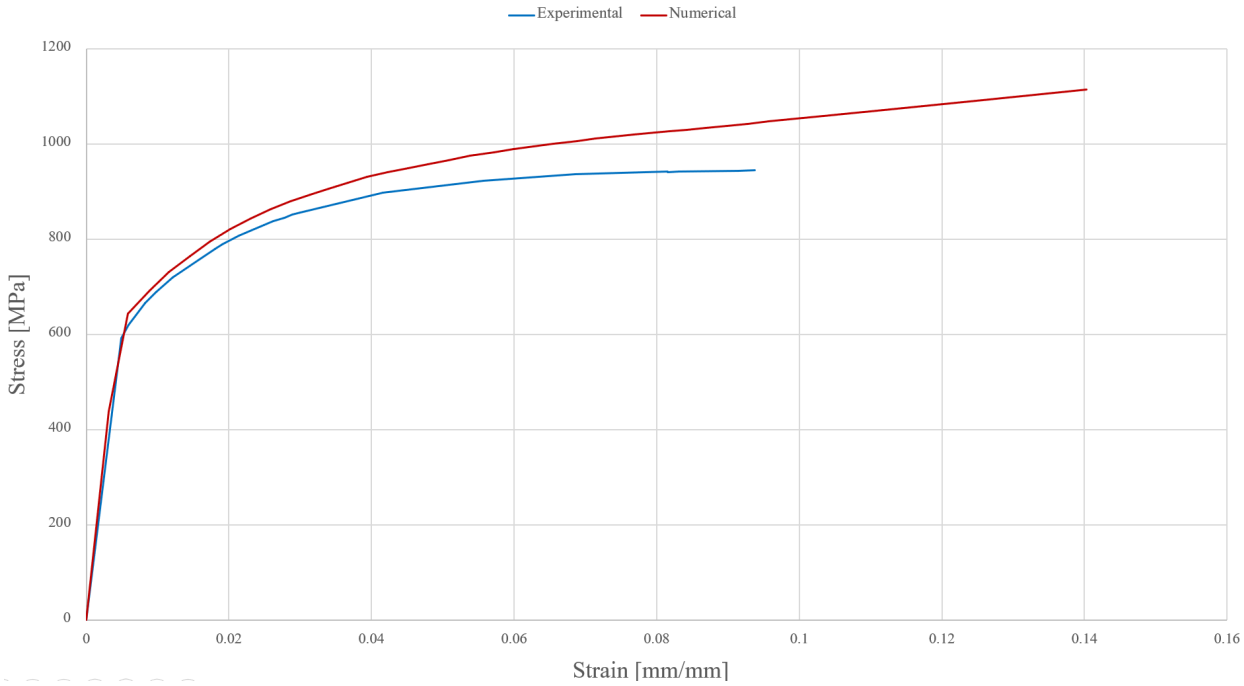

Figure 5.6: Stress vs strain results of both numerical and experimental results for specimen 6Ha.

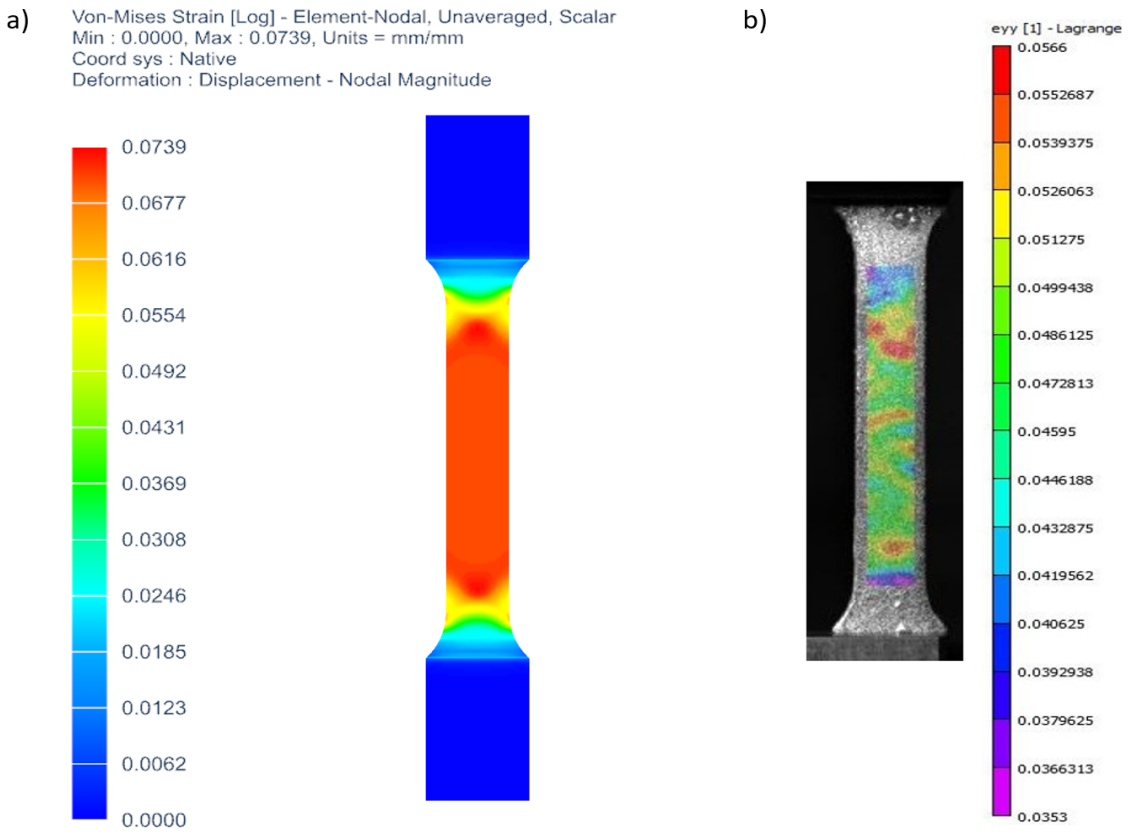

Figure 5.7: Strain distribution of specimen 1Lc for a displacement of approximately 4.916 obtained from: a) FEM model; b) DIC.

After analysing and comparing Figures 5.7 a) and b), it is obvious that strain distribution is different between the two. In the FE simulation, the middle part of the specimen is all under similar values of

strain, being this equally distributed. As for the experimental test, the middle section of the specimen presents some stress concentration areas where strain values are much higher than in the rest. This behaviour points to the existence of stress concentration features, such as porosity, roughness, etc, which will further affect the specimens tensile behaviour.

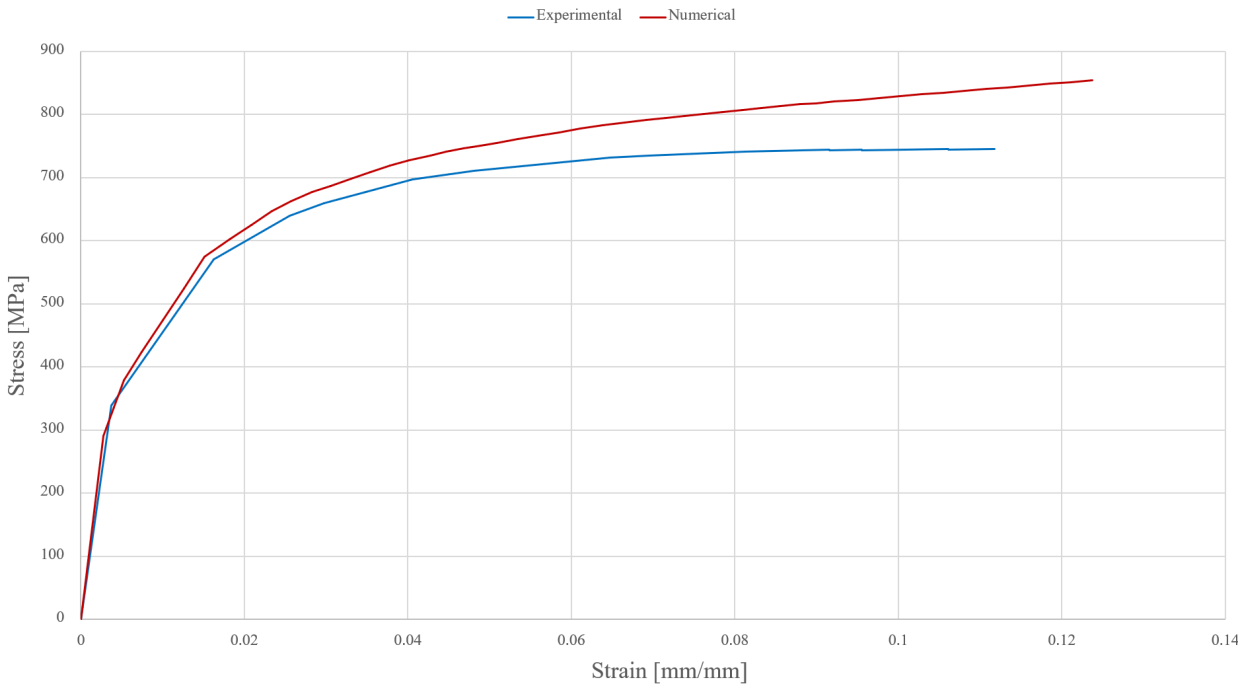

Figure 5.8: Stress vs strain results of both numerical and experimental results for specimen 1Lc.

Analysing the chart in Figure 5.8, the numerical results present a good approximation to the experimental ones. A conclusion to take would be that despite the discrepancy is not glaring, the the numerical results are closer to the experimental ones for specimen 1Lc than in specimen 6Ha, in Figure 5.6. The usage of DIC to conduct strain measurement of specimen 1Lc can be associated with this better approximation.

Chapter 6

Conclusions

6.1 Achievements

In this work, an investigation on the mechanical performance of WAAM specimens was conducted to better understand how the particular characteristics of this method would influence the specimen's behaviour. Different heat input sets and specimen location along the deposition height of the wall structure were compared for the various parameters accessed.

Hardness measurements showed that in fact deposited material located in the base of the wall structure presented higher hardness than the material deposited in subsequent layers, which was in accordance with previous studies. Low Heat input set specimens presented higher hardness values than the ones from the High Heat input set leading to the hypothesis of a more homogeneous and refined grain structure, in the prior specimens. These results impact on mechanical properties was only spotted for maximum strain between heat input sets, with the HH presenting a much lower value.

Microstructural observations confirmed what hardness measurements had presented, with the LH input set specimens having smaller and more refined grains than the HH input set. Regarding the evolution of the grain structure along with the height of the wall, there was not a clear conclusion to be drawn, with grains maintaining a similar size. The appearance of elongated grains due to the temperature gradient felt during material deposition was also noticed, as expected, with a more distinct presence in the base specimens and a natural fade away as the height increased.

Specimen anisotropy was also evident, with differently orientated faces showing distinct microstructures.

Regarding the tensile loading tests performed, the specimens belonging to the HH input set presented a significantly lower maximum strain when compared to the ones from the LH input set. This was directly related to the microstructural observations, where LH input set specimens evinced a more refined grain structure and hence presenting higher values for maximum strain. For the same parameter, but this time considering the different wall locations, in a first analysis, which considered all tested specimens (except 1La), the outcome did not have a reasoned pattern and no conclusions could be drawn. Results from DIC tested specimens were isolated as a way to inquire if this more accurate strain

measuring method could uncover any potential experimental errors. These maximum strain values were very different from the previous ones, with little to no variation being noticed along the wall structure's height, evincing the previously observed microstructure characteristics.

Ultimate tensile strength was found to be similar between different Heat input sets. This parameter only showed a slight discrepancy regarding 'a' specimens, which presented a higher value in comparison to the others. This is thought to be due to the marginal increase in grain refinement in this part of the wall which, by means of fine-grain strengthening mechanisms, inflated the value of UTS. When comparing the value of UTS for the wire material ($\sigma_U = 980$ MPa) with the mean values obtained (LH: $\sigma_U = 908.7$ MPa; HH: $\sigma_U = 912.4$ MPa) it is safe to assume that the deposited material presents good strength. Toughness was found to have a similar variation to the maximum strain given that the values for UTS were very similar between specimens.

Regarding yield strength, the main point to be noted here is the large difference registered between the wire material ($\sigma_{yield} = 890$ MPa) and the deposited material ($\sigma_{yield} = 571.7$ MPa). The latter was not able to fulfill a decent approximation.

Fatigue tests results presented a high level of dispersion, in terms of fatigue life, for the same load levels, despite the small number of specimens tested. Phenomena, such as secondary hardening, are believed to be the causes of this occurrence.

Fractography analysis confirmed what was observed during microstructure analysis, with LH input specimens having a more refined microstructure than the HH input ones. It also enabled the characterization of specimen fracture as ductile, due to the presence of striations.

Lastly, the FEM models showed a good approximation between the numerical and experimental results. Also, the stress distribution of tested specimens was clearly affected by material imperfections. This was confirmed when comparing the strain map of the FEM model and the DIC.

6.2 Future Work

Taking into account that WAAM is a relatively new technology, there are a lot of investigation paths that can be pursued with the aim of better understanding and improving this method and ultimately making it attractive for aerospace manufacturers.

Regarding this work, similar studies can be performed to complement its achievements. The measurement of residual stresses on the produced structures should be the next step. For the same material and testing conditions, specimen orientation influence can be studied to access the isotropy, in terms of mechanical performance, of the built structure. LCF tests should also be carried out and for a larger number of specimens with the intent to figure out if in fact a secondary hardening happens for a certain strain range.

In this dissertation, the FEM models constructed were only complementary, meaning they only had the aim of confirming the expected results. More complex and exact models can be produced to better characterize the behaviour of the samples.

Other specimen geometries and materials can also be studied in future works, with the purpose of

better understanding this method.

Also, the environmental impact of this process should be investigated in detail and ways to reduce it be formulated. Being a non-subtracting method, as it adds material instead of taking it to form a part, it presents almost no waste, which makes it well forwarded towards being a more sustainable alternative to more traditional techniques.

Production time is too a major setback of this technique and can raise some doubts from the manufacturers. Hereupon, a more systematic development will be required to reduce it.

References

[1] T. Wohlers and T. Gornet. History of additive manufacturing. http://wohlersassociates.com/history2014.pdf. accessed: 14.12.2020.

[2] W. J. Sames, F. A. List, S. Pannala, R. R. Dehoff, and S. S. Babu. The metallurgy and processing science of metal additive manufacturing. *International Materials Reviews*, 61(5):315–360, 2016.

[3] AMFG. An Introduction to Wire Arc Additive Manufacturing [2020 Update]. https://amfg.ai/2018/05/17/an-introduction-to-wire-arc-additive-manufacturing/, . accessed: 11.9.2020.

[4] AMFG. Metal 3D Printing: What is Direct Energy Deposition? https://amfg.ai/2018/09/27/metal-3d-printing-what-is-direct-energy-deposition/, . accessed: 15.9.2020.

[5] M. K. Thompson, G. Moroni, T. Vaneker, G. Fadel, R. I. Campbell, I. Gibson, A. Bernard, J. Schulz, P. Graf, B. Ahuja, and F. Martina. Design for additive manufacturing: Trends, opportunities, considerations, and constraints. *CIRP Annals - Manufacturing Technology*, 65:737–760, 2016.

[6] Huisman. Equiped for Impact. https://www.huismanequipment.com/en/about_huisman/huisman__innovation. accessed: 5.12.2020.

[7] M. Aysha. NASA 3D prints a rocket engine for its Artemis exploration mission. https://www.3dnatives.com/en/nasa-3d-printed-rocket-parts-150920204/. accessed: 6.12.2020.

[8] T. D. Ngoa, A. Kashania, G. Imbalzanoa, K. T. Nguyena, and D. Hui. Additive manufacturing (3d printing): A review of materials, methods, applications and challenges. *Composites Part B*, 143: 172–196, 2018.

[9] S. A. Tofail, E. P. Koumoulos, A. Bandyopadhyay, S. Bose, L. O'Donoghue, and C. Charitidis. Additive manufacturing: scientific and technological challenges, market uptake and opportunities. *Materials Today*, 21(1):22–37, 2018.

[10] D. Herzog, V. Seyda, E. Wycisk, and C. Emmelmann. Additive manufacturing of metals. *Acta Materialia*, 117:371–392, 2016.

[11] F. Martina and S. Williams. *Wire+arc additive manufacturing vs. traditional machining from solid: a cost comparison*. Cranfield University, version 1.0 edition, April 2015.

[12] WAAMMAT. WIRE + ARC ADDITIVE MANUFACTURING. https://waammat.com/about/waam. accessed: 14.9.2020.

[13] B. Wu, Z. Pan, D. Ding, D. Cuiuri, H. Li, J. Xu, and J. Norrish. A review of the wire arc additive manufacturing of metals: properties, defects and quality improvement. *Journal of Manufacturing Processes*, 35:127–139, 2018.

[14] C. Bourlet, S. Zimmer-Chevret, R. Pesci, R. Bigot, A. Robineau, and F. Scandella. Microstructure and mechanical properties of high strength steel deposits obtained by wire-arc additive manufacturing. *Journal of Materials Processing Tech.*, 285:1–13, 2020.

[15] S. R. Singh and P. Khanna. Wire arc additive manufacturing (WAAM): A new process to shape engineering materials. *Materials Today: Proceedings*, 2020.

[16] J. Xiong, Y. Lei, H. Chen, and G. Zhang. Fabrication of inclined thin-walled parts in multi-layer single-pass gmaw-based additive manufacturing with flat position deposition. *Journal of Materials Processing Technology*, 240:397–403, 2017.

[17] M. Dinovitzer, X. Chen, J. Laliberte, X. Huang, and H. Frei. Effect of wire and arc additive manufacturing (WAAM) process parameters on bead geometry and microstructure. *Additive Manufacturing*, 26:138–146, 2019.

[18] J. C. G. Lopes. Feasibility of the milling process on HSLA parts manufactured with Wire and arc additive manufacturing. Master's thesis, Faculdade de Ciências e Tecnologia da Universidade Nova de Lisboa, 2019.

[19] V. A. Hosseini, M. Högström, K. Hurtig, M. A. V. Bermejo, L. Stridh, and L. Karlsson. Wire-arc additive manufacturing of a duplex stainless steel: thermal cycle analysis and microstructure characterization. *Welding in the World*, 63:975–987, 2019.

[20] T. A. Rodrigues, V. Duarte, R. M. Miranda, T. G. Santos, and J. P. Oliveira. Current Status and Perspectives on Wire and Arc Additive Manufacturing (WAAM). *Materials*, 12(1121):1–41, 2019.

[21] M. Easton, M. Qian, A. Prasad, and D. StJohn. Recent advances in grain refinement of light metals and alloys. *Current Opinion in Solid State and Materials Science*, 20:13–24, 2016.

[22] Y. Dai, S. Yu, A. Huang, and Y. Shi. Microstructure and mechanical properties of high-strength low alloy steel by wire and arc additive manufacturing. *International Journal of Minerals, Metallurgy and Materials*, 27(7):933–942, 2020.

[23] E. Aldalur, F. Veiga, A. Suarez, J. Bilbao, and A. Lamikiz. High deposition wire arc additive manufacturing of mild steel: Strategies and heat input effect on microstructure and mechanical properties. *Journal of Manufacturing Processes*, 58:615–626, 2020.

[24] T. A. Rodrigues, V. Duarte, J. A. Avila, T. G. Santos, R. Miranda, and J. Oliveira. Wire and arc additive manufacturing of HSLA steel: Effect of thermal cycles on microstructure and mechanical properties. *Additive Manufacturing*, 27:440–450, 2019.

[25] W. J. Sames, F. A. List, S. Pannala, R. R. Dehoff, and S. S. Babu. The metallurgy and processing science of metal additive manufacturing. *International Materials Reviews*, 61(5):315–360, 2016.

[26] J. Ding, P. Colegrove, J. Mehnen, S. Ganguly, P. S. Almeida, F. Wang, and S. Williams. Thermo-mechanical analysis of Wire and Arc Additive Layer Manufacturing process on large multi-layer parts. *Computational Materials Science*, 50:3315–3322, 2011.

[27] M. P. Mughal, H. Fawad, R. A. Mufti, and M. Siddique. Deformation modelling in layered manufacturing of metallic parts using gas metal arc welding: effect of process parameters. *Modelling and Simul. Mater. Sci. Eng.*, 13:1187–1204, 2005.

[28] P. A. Colegrove, J. Donoghue, F. Martina, J. Gu, P. Prangnell, and J. Hönnige. Application of bulk deformation methods for microstructural and material property improvement and residual stress and distortion control in additively manufactured components. *Scripta Materialia*, 135:111–118, 2017.

[29] A. Busachi, J. Erkoyuncu, P. Colegrove, F. Martina, and J. Ding. Designing a WAAM Based Manufacturing System for Defence Applications. *Procedia CIRP*, 37:48–53, 2015.

[30] R. Biswal, X. Zhang, A. K. Syed, M. Awd, J. Ding, F. Walther, and S. Williams. Criticality of porosity defects on the fatigue performance of wire + arc additive manufactured titanium alloy. *International Journal of Fatigue*, 122:208–217, 2019.

[31] J. Gu, J. Bai, J. Ding, S. Williams, L. Wang, and K. Liu. Design and cracking susceptibility of additively manufactured Al-Cu-Mg alloys with tandem wires and pulsed arc. *Journal of Materials Processing Tech.*, 262:210–220, 2018.

[32] A. Caballero, J. Ding, S. Ganguly, and S. Williams. Wire + Arc Additive Manufacture of 17-4 PH stainless steel: Effect of different processing conditions on microstructure, hardness, and tensile strength. *Journal of Materials Processing Tech.*, 268:54–62, 2019.

[33] F. Wang, S. Williams, P. Colegrove, and A. A. Antonysamy. Microstructure and Mechanical Properties of Wire and Arc Additive Manufactured Ti-6Al-4V. *Metallurgical and Materials Transactions A*, 44A:968–977, 2013.

[34] J. V. Gordon and D. G. Harlow. Statistical Modeling of Wire and Arc Additive Manufactured Stainless Steel 304: Microstructure and Fatigue. *International Journal of Reliability, Quality and Safety Engineering*, 26(4):1–13, 2019.

[35] S. Beretta and S. Romano. A comparison of fatigue strength sensitivity to defects for materials manufactured by AM or traditional processes. *International Journal of Fatigue*, 94:178–191, 2016.

[36] P. Qvale and G. Härkegård. A simplified method for weakest-link fatigue assessment based on finite element analysis. *International Journal of Fatigue*, 100:78–83, 2017.

[37] G. Härkegård and G. Halleraker. Assessment of methods for prediction of notch and size effects at the fatigue limit based on test data by Böhm and Magin. *International Journal of Fatigue*, 32: 1701–1709, 2010.

[38] P. Dirisu, G. Supriyo, F. Martina, X. Xu, and S. Williams. Wire plus arc additive manufactured functional steel surfaces enhanced by rolling. *International Journal of Fatigue*, 130, 2020.

[39] Weldwire. Product Specification. `http://www.weldwire.net/wp-content/uploads/2013/07/110S-G.pdf`. accessed: 18.11.2020.

[40] N. M. de Carvalhal Soares. Mechanical behavior characterization of planar and non-planar sandwich composite panels with agglomerated cork core. Master's thesis, Instituto Superior Técnico, 2017.

[41] J. Colin, A. Fatemi, and S. Taheri. Cyclic hardening and fatigue behavior of stainless steel 304l. *J Mater Sci*, 46:145–154, 2011.

[42] J. Zhou, Z. Sun, P. Kanouté, and D. Retraint. Experimental analysis and constitutive modelling of cyclic behaviour of 316l steels including hardening/softening and strain range memory effect in lcf regime. *International Journal of Plasticity*, 107:54–78, 2018.

[43] L. Xu, S. Yang, L. Zhao, Y. Han, H. Jing, and K. Wang. Low cycle fatigue behavior and microstructure evolution of a novel fe-22cr-15ni austenitic heat-resistant steel. *Journal of Materials Research and Technology*, 9:14388–14400, 2020.

[44] I. Dzioba and S. Lipiec. Fracture mechanisms of s355 steel—experimental research, fem simulation and sem observation. *Materials*, 12, 2019.

[45] T. E. Toolbox. Poisson's Ratio. `https://www.engineeringtoolbox.com/poissons-ratio-d_1224.html`. accessed: 8.12.2020.

Appendix A

Fractography Analysis Images

In this appendix, relevant pictures from other specimens analysed in the fractography analysis are presented.

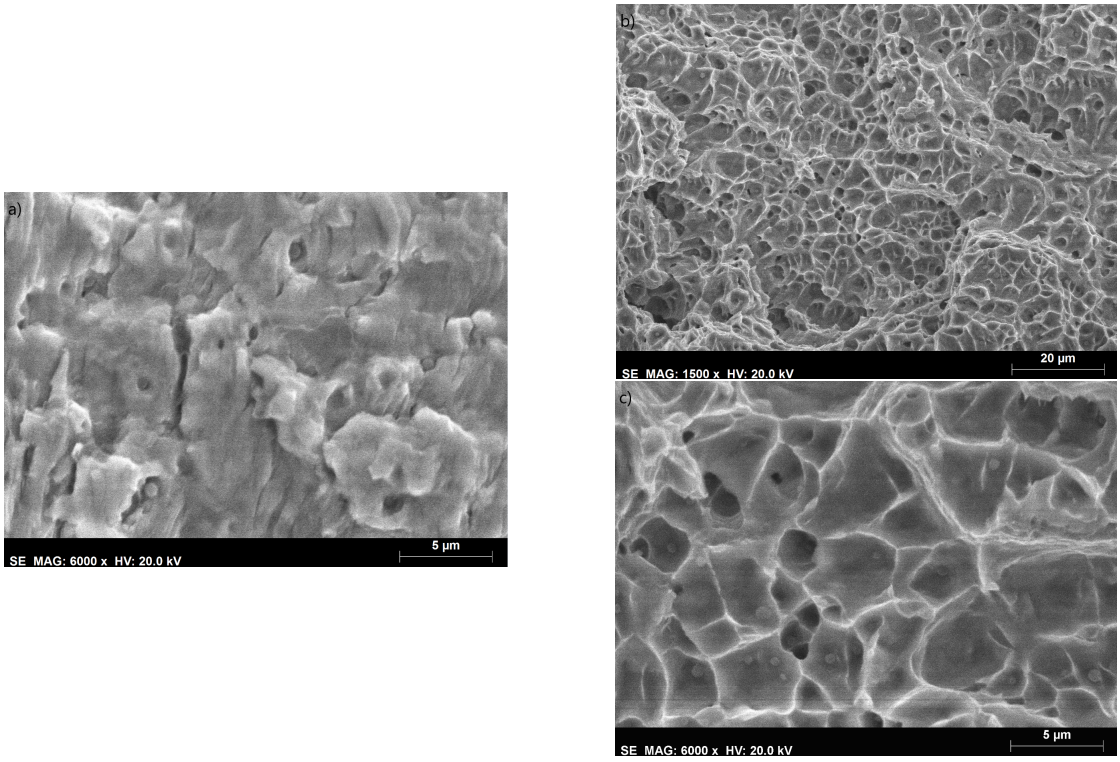

Figure A.1: Detailed view of: specimen 8Lb microstructure at the primary fracture surface under an amplification of a) x6000; specimen 8Lb microstructure outside the fracture surface under an amplification of b) x1500; and c) x6000.

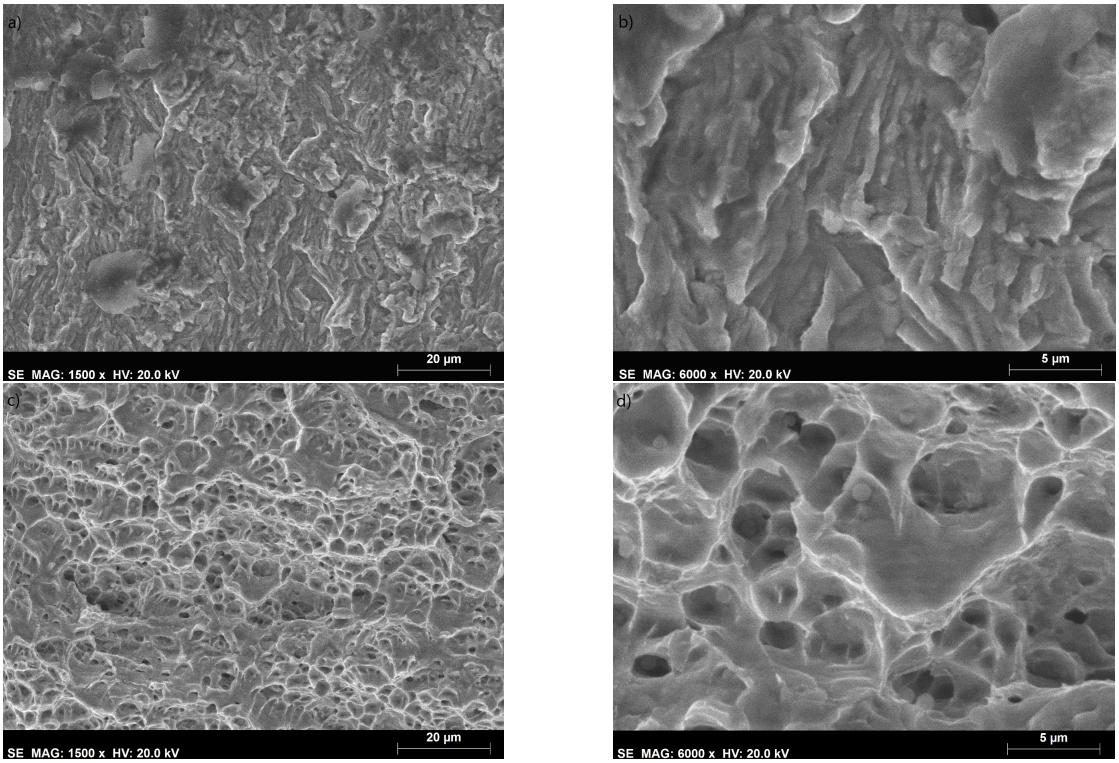

Figure A.2: Detailed view of: specimen 9Lc microstructure at the primary fracture surface under an amplification of a) x1500 b) x6000; specimen 9Lc microstructure outside the fracture surface under an amplification of c) x1500; and d) x6000.

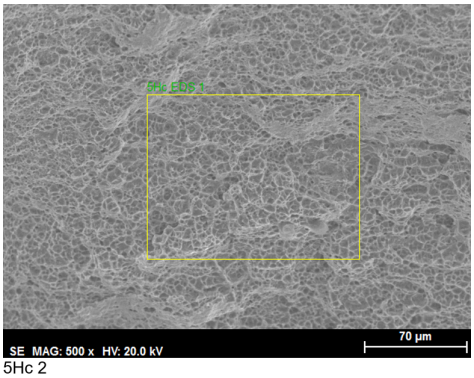

5Hc 2
Date:28-10-2020 11:49:37
Image size:2000 x 1500
Mag:500x
HV:20.0kV

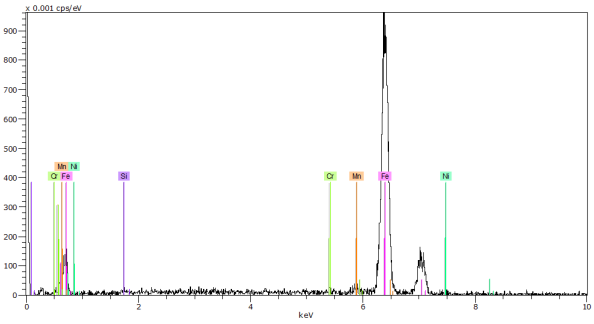

5Hc EDS 1.xls Date:28-10-2020 11:50:08 HV:20.0kV Puls th.:0.45kcps

El	AN	Series	unn. C [wt.%]	norm. C [wt.%]	Atom. C [at.%]	Error (1 Sigma) [wt.%]
Fe	26	K-series	220.06	96.86	96.54	6.44
Mn	25	K-series	2.64	1.16	1.18	0.28
Ni	28	K-series	2.42	1.06	1.01	0.35
Si	14	K-series	0.75	0.33	0.65	0.15
Cr	24	K-series	1.32	0.58	0.62	0.17
		Total:	227.19	100.00	100.00	

Figure A.3: Analysis of the specimen 5Hc chemical composition.